**What dynamics drive future wind scenarios for coastal upwelling off Peru and Chile?**

Ali Belmadani[1,2,3], Vincent Echevin[1], Francis Codron[4], Ken Takahashi[5], and Clémentine Junquas[5,6]

[1] Laboratoire d'Océanographie et du Climat: Expérimentations et Approches Numériques (LOCEAN), Institut de Recherche pour le Développement (IRD), Institut Pierre-Simon Laplace (IPSL), Université Pierre et Marie Curie (UPMC), Paris, France

[2] International Pacific Research Center (IPRC), School of Ocean and Earth Science and Technology (SOEST), University of Hawaii at Manoa, Honolulu, Hawaii

[3] Department of Geophysics (DGEO), Faculty of Physical and Mathematical Sciences (FCFM), Universidad de Concepcion (UdeC), Concepcion, Chile

[4] Laboratoire de Météorologie Dynamique (LMD), IPSL, UPMC, Paris, France

[5] Instituto Geofisico del Peru (IGP), Lima, Peru

[6] IRD / UJF-Grenoble 1 / CNRS / G-INP, LTHE UMR 5564, Grenoble, France

Revised for *Climate Dynamics*

November 28th, 2013

[1] *Corresponding author address*: Ali Belmadani, DGEO, FCFM, Universidad de Concepcion, Avda. Esteban Iturra s/n - Barrio Universitario, Casilla 160-C, Concepcion, Chile. E-mail: abelmadani@dgeo.udec.cl. Phone: +56-41-220-3111.

## Abstract

The dynamics of the Peru-Chile Upwelling System (PCUS) are primarily driven by alongshore wind stress and curl, like in other eastern boundary upwelling systems. Previous studies have suggested that upwelling-favorable winds would increase under climate change, due to an enhancement of the thermally-driven cross-shore pressure gradient. Using an atmospheric model on a stretched grid with increased horizontal resolution in the PCUS, a dynamical downscaling of climate scenarios from a global coupled general circulation model (CGCM) is performed to investigate the processes leading to sea-surface wind changes. Downscaled winds associated with present climate show reasonably good agreement with climatological observations. Downscaled winds under climate change show a strengthening off central Chile south of 35°S (at 30–35°S) in austral summer (winter) and a weakening elsewhere. An alongshore momentum balance shows that the wind slowdown (strengthening) off Peru and northern Chile (off central Chile) is associated with a decrease (an increase) in the alongshore pressure gradient. Whereas the strengthening off Chile is likely due to the poleward displacement and intensification of the South Pacific Anticyclone, the slowdown off Peru may be associated with increased precipitation over the tropics and associated convective anomalies, as suggested by a vorticity budget analysis. On the other hand, an increase in the land-sea temperature difference is not found to drive similar changes in the cross-shore pressure gradient. Results from another atmospheric model with distinct CGCM forcing and climate scenarios suggest that projected wind changes off Peru are sensitive to concurrent changes in sea surface temperature and rainfall.


## 1. Introduction

Eastern boundary upwelling systems are vast regions of the coastal ocean found in both hemispheres along the western shores of continents bordering the Pacific and Atlantic Oceans. They are characterized by upwelling of cold, nutrient-rich waters that sustain high biological productivity [*Chavez*, 1995] and the world's most productive fisheries [*Fréon et al.*, 2009]. In particular, the Peru-Chile Upwelling System (PCUS), the eastern boundary upwelling system of the South Pacific Ocean, stands out with fish catch per unit area an order of magnitude larger than in the other eastern boundary upwelling systems [*Chavez et al.*, 2008] and with the second largest fish production in the world ocean, accounting for over 12% of the world fisheries [*Food and Agriculture Organization*, 2010]. In this context, how the PCUS will respond to global warming appears as a key question from both the scientific and the societal points of view.

In the PCUS and other eastern boundary upwelling systems, upwelling-favorable conditions are mainly set by alongshore trade wind stress, which varies along the coast associated with nearshore wind drop-off zones, expansion fans off capes in supercritical conditions, and other effects of coastal topography [e. g. *Winant et al.*, 1988; *Capet et al.*, 2004], although Ekman suction induced by cyclonic wind stress curl could also have an important contribution [*Albert et al.*, 2010]. The future changes in alongshore wind and wind stress curl may be driven by various mechanisms operating on a range of spatial scales. Nearshore equatorward winds are embedded in the eastern branch of the South Pacific Anticyclone (SPA), which is also the lower branch of the Hadley cell. Both observations [*Johanson and Fu*, 2009] and coupled general circulation model (CGCM) projections [*Lu et al.*, 2007; *Previdi and Liepert*, 2007; *Gastineau et al.*, 2008; *Johanson and Fu*, 2009] support a poleward expansion of the Hadley cell with global warming, with a likely impact on the latitudinal distribution of upwelling-favorable winds in the PCUS. On the other hand, while the Hadley cell tends to weaken in climate change simulations [*Held and Soden*, 2006; *Lu et al.*, 2007; *Vecchi and Soden*, 2007; *Gastineau et al.*, 2008, 2009], this model trend is weak [*Vecchi and Soden*, 2007] and reanalysis data does not show any significant change in the southern hemisphere over recent decades [*Mitas and Clement*, 2005], leaving the future of the Hadley cell strength open to debate and its possible influence on nearshore winds unclear.

Besides, the low-level atmospheric circulation in the northern PCUS exhibits a separation of the eastern branch of the SPA into tropical Pacific easterly trade winds and westerlies flowing over the Gulf of Panama [*Strub et al.*, 1998]. The former are associated with the Walker circulation, which presents a weakening in both observations [*Vecchi et al.*, 2006; *Tokinaga et al.*, 2012a] and CGCMs [*Vecchi et al.*, 2006; *Vecchi and Soden*, 2007; *Tokinaga et al.*, 2012b]. One may argue that such slowdown should cause upwelling-favorable winds to weaken, but the connection between the two systems is relatively weak, and instead, the upwelling-favorable winds have been seen to increase off Peru during El Niño events [*Wyrtki, 1975; Enfield 1981; Bakun and Weeks*, 2008].

On longer time scales, regional processes may also play an important role. Although the positive trend in upwelling-favorable ship-borne wind presented by *Bakun* [1990] over the last decades in four eastern boundary upwelling systems including the PCUS may not be significant for the Peruvian coast once the necessary corrections are applied for changes in measuring practices and anemometer heights [*Cardone et al*., 1990; *Tokinaga and Xie*, 2011], this trend appears to exist off central Chile (Fig. 1), consistent with QuikSCAT satellite measurements over 2000–2007 [*Demarcq*, 2009]. Indirect evidence for a possible strengthening of the upwelling-favorable winds is provided by a negative trend in coastal SST, which has been observed off northern Chile since at least 1979 [*Falvey and Garreaud*, 2009] and off central-southern Peru since the mid-twentieth century [*Gutiérrez et al*, 2011]. However, it should be considered that natural decadal variability could also be an important contributor to the trends [e. g. *Vargas et al.*, 2007], so the issue of attribution is an open question.

A possible strengthening of the wind off central Chile with global warming is understood to be the result of large-scale changes in the subtropical high-pressure bands and their interaction with the Andes [e. g. *Garreaud and Falvey*, 2009]. For the tropical eastern South Pacific, mechanisms may be more local and subtle. For instance, land-sea thermal gradients associated with changes in coastal cloudiness [*Enfield*, 1981; *Vargas et al*., 2007] and enhanced land heating by greenhouse gas forcing [*Bakun*, 1990; *Sutton et al.*, 2007] have been proposed to lead to the enhancement of geostrophic alongshore wind. On the other hand, alongshore pressure gradients associated with sea surface temperature (SST) anomalies, e.g. during El Niño, can also drive alongshore coastal wind anomalies [*Quijano-Vargas*, 2011; Takahashi, K., A. G. Martínez, and K. Mosquera-Vásquez, The very strong 1925-26 El Niño in the far eastern Pacific, revisited, *Clim. Dyn.*, in prep.]. Furthermore, wind, SST, and the intertropical convergence zone (ITCZ) are dynamically linked in this region and thus compose a coupled system [e. g. *Xie and Philander*, 1994; *Takahashi and Battisti*, 2007a]. Thus, it may not be adequate, for instance, to attribute the changes in winds as a result of the changes in SST or the ITCZ unless a mechanism involving an external forcing can be identified, such as orographic forcing [e. g. *Xu et al.*, 2004; *Takahashi and Battisti*, 2007a; *Sepulchre et al.*, 2009] or changes in the Atlantic meridional overturning circulation [e.g. *Zhang and Delworth*, 2005]. Other feedbacks involving low-level clouds could also be playing a role through their albedo [*Philander et al*., 1996; *Takahashi and Battisti*, 2007a] or cloud-top cooling [*Nigam*, 1997].

There have been recent attempts to assess changes in the low-level atmospheric circulation in the PCUS at the regional scale. *Garreaud and Falvey* [2009] found an increase in SPA intensity and equatorward winds off Chile in an ensemble of 15 CGCMs. However, the coarse resolution of these models (table 1) does not allow extrapolating the results to upwelling-favorable winds in the nearshore drop-off zone. To overcome this issue, the authors performed a dynamical downscaling of the UKMO-HadCM3 CGCM [*Pope et al.*, 2000; *Gordon et al.*, 2000] using the PRECIS regional climate model [*Jones et al.*, 2004] and consistently found a summer increase in alongshore winds off central Chile. On the other hand, whereas most CGCMs tend to agree in the projected increase in southerly flow off central Chile, there is significant discrepancy in the response of equatorward winds off Peru and northern Chile, with perhaps a slight tendency toward reduced winds in summer off northern and central Peru (Fig. 2). *Goubanova et al.* [2011] performed a statistical downscaling of PCUS surface winds from the IPSL-CM4 CGCM [*Hourdin et al.*, 2006; *Marti et al.*, 2010] and found a 10–20% increase in the mean alongshore wind off Chile and a ~10% decrease in the summer alongshore wind off Peru with quadrupling of carbon dioxide ($CO_2$) concentrations (the so-called "1pctto4x" scenario [*Nakicenovic et al.*, 2000], hereafter $4CO_2$) compared to preindustrial levels (the so-called "PIcntrl" scenario, hereafter PI), in qualitative agreement with CGCM response (Fig. 2). They also found a 10–20% wind stress curl increase (decrease) in winter (summer) off Peru and a year-round increase of up to 50% off Chile south of 25°S. The authors interpreted the wind and wind stress curl increase off Chile as the result of a strengthening of the large-scale meridional pressure gradient over the subtropical eastern South Pacific and the decrease off Peru as a consequence of both the slowdown of the Walker circulation and the poleward extension of the Hadley cell. In the California Upwelling System, *Snyder et al.* [2003] downscaled the NCAR-CCSM CGCM

[*Boville and Gent*, 1998] using the RegCM2.5 regional climate model [*Snyder et al.*, 2002] with nearly a doubling of $CO_2$ concentrations (the so-called "1pctto2x" scenario, hereafter $2CO_2$) compared to modern levels and found an increase in cyclonic wind stress curl off northern California during the upwelling season with moderate changes in seasonality, and inconclusive results for the central California coast. They related the increase in the northern region to a strengthening of the land-sea temperature gradient, in agreement with *Bakun* [1990]'s hypothesis.

In this paper, a global circulation model (GCM) with locally high resolution over the PCUS is used to perform a dynamical downscaling of the impacts of global warming on surface winds off the coasts of Peru (4°S–18°S) and Chile (18°S–40°S). In addition, a second configuration of the same GCM with a different experimental setup is used to assess the robustness of the surface wind response. The approach is similar to *Garreaud and Falvey* [2009] but uses different models and climate scenarios. Furthermore, the study domain extends over the whole PCUS, allowing to assess and contrast the different responses of the Peru and Chile regions. The paper is organized as follows: in the next section, the models and data used in this study are described. The results of the downscaled climate change simulations are presented in section 3. Last, a summary of the results followed by a discussion are proposed in section 4.

## 2. Models and data

### 2.1 Main GCM setup (LMDz-ESP05)

The GCM used for the dynamical downscaling is LMDz from the Laboratoire de Météorologie Dynamique [*Hourdin et al.*, 2006]. LMDz is an atmospheric GCM with a variable resolution or "zooming" capability. The model has 19 hybrid sigma-pressure levels in the vertical. It has no active microphysics scheme. A Mellor-Yamada parameterization is used for the boundary layer with a moist thermal plume scheme. Thermal and evapo-transpiration processes over continental surfaces in the model are described by *Hourdin et al.* [2006].

The main atmospheric configuration of LMDz has a global 4.9°x2.4° coarse-resolution grid, that is progressively refined to a higher 0.5°x0.5° horizontal resolution in the PCUS region (99°W–61°W,36°S–6°N; Fig. 3a). It will be hereafter called LMDz-ESP05, to highlight the zoomed region and resolution. LMDz in that configuration exhibits reasonably realistic behavior in the PCUS, especially in terms of low clouds and boundary layer structure [*Wyant et al.*, 2010]. The model is run over 10-year periods, after discarding a one-year adjustment period, for climate states with different $CO_2$ concentrations and prescribed SST. Note that in contrast to many downscaling experiments with regional models, the LMDz-ESP05 model is global and does not use nudging outside of the PCUS region. The outputs are saved daily.

Four scenarios are considered in this study: present-day, $4CO_2$, $2CO_2$, and PI. Climatological SST and sea ice over 1979–1999 from the Atmospheric Model Intercomparison Project (AMIP) merged observational dataset [*Hurrell et al.*, 2008], and $CO_2$ concentrations corresponding to the 20$^{th}$ century (the so-called "20C3M" scenario) are used for the present-day control run (CR). For the other scenarios, different $CO_2$ concentrations are used, and SST anomalies coming from CGCM experiments (relative to 20C3M climatology) are added to the AMIP climatology. CGCM SST are not used directly to alleviate the large biases in the PCUS region [e.g. *Large and Danabasoglu*, 2006].

The SST anomalies for the different scenarios are obtained from the IPSL-CM4 CGCM, run with the same $CO_2$ concentrations for the CMIP3 experiments. IPSL-CM4 was chosen for five reasons: 1) its mean response to global warming in terms of SST, sea level pressure and surface winds is very similar to that of the Coupled Model Intercomparison Project phase 3

(CMIP3) multimodel ensemble mean [*Goubanova et al.*, 2011; *Echevin et al.*, 2012; Fig. 2]; 2) it represents reasonably well large-scale climate features of importance for the PCUS such as ENSO dynamics [*Belmadani et al.*, 2010] and the SPA [*Garreaud and Falvey*, 2009]; 3) its atmospheric model core is the same as that of LMDz-ESP05, ensuring a dynamical consistency between the CGCM and the GCM; 4) it was the CGCM chosen by *Goubanova et al.* [2011] to downscale future surface winds in the PCUS, so that the comparison of the results from the present study with those of *Goubanova et al.* [2011] may be used to highlight differences between dynamical and statistical downscaling methods; 5) this CGCM, coupled with a biogeochemical model, achieved the highest skill score (based on an evaluation of primary production) in the eastern South Pacific, among a set of four global biogeochemical models [*Steinacher et al., 2010*].

The outputs from the stabilized $4CO_2$ and $2CO_2$ LMDz-ESP05 runs are compared to those from the PI run to assess the impact of global warming on PCUS winds. $4CO_2$ and $2CO_2$ runs are also compared to assess the linearity of the PCUS wind response. Outputs from the CR are directly comparable to present observations and are used for the GCM validation.

**2.2 Complementary validation experiments (LMDz-SA1)**

To assess the sensitivity of the downscaled wind response to the chosen models and climate scenarios, an existing and distinct configuration of LMDz, hereafter called LMDz-SA1, is used as a second dynamical downscaling tool [*Junquas et al.*, 2013]. This configuration uses a zoomed grid over the whole South American continent (96.4°W–13.6°W,63.9°S–18.9°N), with lower resolution both inside (1°x1°) and outside (8°x2.6°) the zoomed region compared to the previously described configuration (Fig. 3b). This variable-resolution model is coupled with another instance of LMDz with globally uniform coarse resolution (3.75°x2.5°), following a two-way nesting technique [*Lorenz and Jacob*, 2005; *Chen et al.*, 2011]: the resulting circulation is determined by the variable-resolution model inside the high-resolution region, and by the regular-grid model outside. As this configuration has been initially developed to study changes in summertime rainfall over Southeastern South America [*Junquas et al.*, 2013], the runs are performed over November through February (NDJF) with different atmospheric initial states, and outputs are averaged over December through February (DJF). As a cautionary notice, since the model runs last only one season, it is not clear whether land air temperature and moisture have time to fully adjust to changes in SST or $CO_2$ concentration. Since land/sea contrast may play a role in the future wind changes [e.g., *Bakun et al.*, 2010], this limits to some extent the comparison with LMDz-ESP05, although the simulations are still useful for assessing the uncertainty in the downscaled scenarios in relation to large-scale changes in SST and atmospheric circulation.

In the LMDz-SA1 CR, both components of the coupled system are forced with AMIP SST and sea-ice. In the so-called FSSTG experiment, the climatological-mean DJF SST differences in a group of 9 CGCMs (which does not include IPSL-CM4) between 2079–2099 in the SRES A1B scenario [*Nakicenovic et al.*, 2000] and 1979–1999 in 20C3M are ensemble-averaged and then added to AMIP to force the coupled system. $CO_2$ concentrations are doubled compared to 20C3M (1979–1999). The 9 CGCMs are identified by *Junquas et al.* [2012] as the most reliable in terms of Southeastern South America precipitation: CCCma CGCM3.1, CCCma CGCM3.1-T63, CSIRO-MK3.0, GFDL CM2.0, GFDL CM2.1, MIROC3.2(hires), MIROC3.2(medres), MIUB-ECHO-G, UKMO-HadCM3. The reader is invited to refer to *Junquas et al.* [2013] for more details on the coupled system, considered here as a GCM for simplicity. The differences between the LMDz-ESP05 and LMDz-SA1 configurations are summarized in Table 2.

### 2.3 CMIP3 models

To put the downscaling results in perspective and discuss regional wind changes in the context of larger-scale trends, a subset of 12 CGCMs from the CMIP3 archive (see table 1) is analyzed in terms of future winds, SST, and rainfall. These CGCMs have been chosen because they are the only ones for which surface winds are available for the $4CO_2$ scenario. The first 100 years of the transient regime during which $CO_2$ concentrations are increased by 1% per year are considered, as the time slots corresponding to stabilized $CO_2$ concentrations were not available for all CGCMs.

### 2.4 Observational data

Observed surface winds are provided by the QuikSCAT-derived Scatterometer Climatology of Ocean Winds (SCOW) [*Risien and Chelton*, 2008], updated over the period September 1999–October 2009 and available on a 0.25°x0.25° grid. The European Centre for Medium-Range Weather Forecasts ERA-Interim reanalysis [*Dee et al.*, 2011], which spans the period 1979–present, is used to assess the vertical structure of the alongshore wind and air temperature near the coasts of Peru and Chile. Compared to most state-of-the-art reanalyses, it has higher horizontal and vertical resolutions (1.5°x1.5° and 37 pressure levels, respectively), making it an appropriate tool to analyze the atmospheric circulation in the vicinity of the steep topography of the Andes.

## 3. Results

### 3.1. Control run validation

To illustrate the impact of high resolution on the low-level circulation, the IPSL-CM4 and LMDz-ESP05 annual mean surface wind fields corresponding to 20C3M and CR are shown in Fig. 4a and 4b, respectively. Also shown is the climatological mean wind from the SCOW (Fig. 4c). The data represents the SPA and the associated eastern branch of alongshore winds. It also captures the nearshore drop-off zone to some extent, as well as the coastal jets near 4°S, 15°S, and 30°S, where the upwelling-favorable winds are locally stronger [*Garreaud and Muñoz*, 2005; *Muñoz and Garreaud*, 2005; *Renault et al.*, 2009, 2012]. Clear biases are seen in the coarse-resolution CGCM outputs, such as a meridionally-confined SPA, overestimated westerlies, and most importantly, poor representation of the drop-off zone, with an overestimated cross-shore scale (up to ~5°) and very weak nearshore winds (<2 m $s^{-1}$) over the whole length of the Peru and Chile shores (Fig. 4a). In fact, the CGCM has a coast well displaced from the actual coastline, which limits the comparison with the SCOW.

On the other hand, LMDz-ESP05 reproduces reasonably well most features of the regional circulation, including the nearshore drop-off zone and the coastal jets (Fig. 4b). Some discrepancies are still found with the SCOW data, namely underestimated trade winds offshore and overestimated winds in the coastal jet areas (except at 4°S), as well as a meridionally slightly narrower SPA. Nevertheless, the clear improvement due to downscaling and the overall consistency with the observed data give us confidence in the GCM surface circulation.

The LMDz-ESP05 CR alongshore wind and temperature cross-shore structures in the central Peru and central Chile coastal jet areas are then assessed against the ERA-Interim reanalysis data (Fig. 5). The focus is on the peak upwelling season, which occurs in winter off Peru and in summer off Chile. At 15°S, the CR coastal jet core is located at ~500 m height within the first 100 km from the coast, with maximum velocities of ~8.5 m $s^{-1}$ and a nearly barotropic structure within the boundary layer (Fig. 5a). The latter is capped by a temperature inversion resulting from the balance of adiabatic heating by subsidence on the eastern flank of the SPA, upward turbulent air transfer influenced by the relatively cold ocean surface, and radiative cooling [e. g., Haraguchi, 1968]. As a result, low-level winds in the boundary layer are decoupled from the winds aloft, which tend to be weak below ~3000 m. The GCM reproduces the reanalysis winds well, although the boundary layer appears slightly deeper in ERA-Interim (Fig. 5b). Off Chile, the coastal jet core is located at 400-600 m and 200-500 m height in the CR and ERA-Interim data, respectively (Figs. 5c-d). These altitudes may be underestimated, as suggested by observations from radiosondes launched from the coastal station of Santo Domingo (33.7°S) during the 15/10/2008-15/11/2008 period as part of the VAMOS Ocean-Cloud-Atmosphere-Land Study Regional Experiment (VOCALS-Rex), which indicate a coastal jet core at 500-1000 m height [Fig. 6h of *Rahn and Garreaud*, 2010]. The GCM appears to overestimate the coastal jet intensity: ~10 m s$^{-1}$, vs ~8.5 m s$^{-1}$ in ERA-Interim and only 2-3 m s$^{-1}$ in radiosonde data [*Rahn and Garreaud*, 2010]. Note that while the discrepancy between ERA-Interim and radiosonde data may be due to the relatively coarse resolution of the reanalysis (1.5°), it may also result from limited sampling of the coastal jet in both space and time. In particular, the soundings were performed in spring rather than summer, during a particular year, and did not allow assessing the geographical location of the coastal jet core. The temperature inversion tends to be shallower in the CR (<500 m) than in ERA-Interim (500-900 m, and up to 1500 m offshore) and in radiosonde data (~600 m, [Figs. 6b, 11a of *Rahn and Garreaud*, 2010]). Overall, the vertical structure in the model is in relatively good agreement with the reanalysis data in both regions. Note that the Andes topography is represented with greater detail in LMDz-ESP05 than in ERA-Interim due to its higher horizontal resolution.

### 3.2 Surface wind response to climate change

Fig. 6 displays the changes in surface winds in the LMDz-ESP05 climate-change scenarios. The focus is on the austral summer and winter seasons, when the changes are most contrasted. During summer, the SPA is located at its southernmost position and is displaced to the south in $2CO_2$ and $4CO_2$ compared to PI, as evidenced by cyclonic (anticyclonic) anomalous circulation north (south) of 35°S (Figs. 6a-b). Off Chile, this displacement generates a weakening of upwelling-favorable winds north of 35°S and a strengthening to the south (Figs. 6a-b). The wind increase south of 35°S (0.5–1 m $s^{-1}$, i.e. 10–20%) does not vary much from $2CO_2$ to $4CO_2$, while the wind decrease to the north in $4CO_2$ (1–2.5 m $s^{-1}$, i.e. 20–40%) is twice that in $2CO_2$ (0.5–1 m $s^{-1}$, i.e. 10–25%). During winter, the SPA moves northward and is also displaced to the south in $2CO_2$ and $4CO_2$ compared to PI (Figs. 6c-d), generating a moderate wind increase near 30°S–35°S (~0.5 m $s^{-1}$ in $2CO_2$ and ~1 m $s^{-1}$ in $4CO_2$, i.e. 10–15% and 30–40%, Figs. 6c-d). To the south and to the north of this localized increase, the alongshore wind decreases, reaching a maximum (~0.5 m $s^{-1}$ in $2CO_2$ and ~1 m $s^{-1}$ in $4CO_2$, i.e. ~5% and ~10%) in the coastal jet near 15°S (south of 35°S the wind is dominantly westerly and the weakening corresponds to anomalous easterlies). Overall, surface winds tend to respond roughly linearly to the increase in $CO_2$, except at a few specific locations (see also Fig. 8a).

Typical LMDz-ESP05 wind stress curl patterns are shown in Fig. 7. Ekman suction (*i.e.* negative wind stress curl) indicates upwelling all along the coasts in a 50–100 km-wide coastal band (~1–2 GCM grid points, Fig. 7a). This intense curl (~5.$10^{-7}$ N $m^{-2}$ near 15°S–17°S) exceeds the observed values (~3.$10^{-7}$ N $m^{-2}$ in QuikSCAT data, *Albert et al.* [2010]). Offshore of this coastal band, upwelling occurs north of ~28°S. South of this limit, positive wind stress curl indicates offshore downwelling. Small-scale positive wind stress curl structures appear south of the coastline orientation change near 15°S. These GCM artifacts, also found in the model seasonal averages (not shown), are not present in QuikSCAT observations (*e.g.* see Fig. 1 in *Albert et al.* [2010]).

Climate change induces a decrease in nearshore Ekman suction north of 30°S (15–20% near 15°S and ~10% near 25°S–30°S in $2CO_2$) and an increase (~40% near 35°S–40°S in $2CO_2$) to the south (Figs. 7b-c). $4CO_2$ changes are about twice larger than $2CO_2$ changes. Overall, these changes roughly coincide with changes in the alongshore wind intensity, which are associated with 15–20% and ~10% decreases in $2CO_2$ alongshore wind stress near 15°S and 30°S, respectively, as well as a ~25% increase near 35°S–40°S, with changes twice larger in $4CO_2$ (not shown). As a result, both Ekman transport and Ekman suction decrease off Peru and northern Chile, whereas the opposite occurs south of 30–35°S. Seasonal variability does not strongly modify these features (not shown).

### 3.3 Momentum budgets and alongshore wind changes

In order to investigate the dynamical processes associated with the surface wind changes, a momentum budget is performed following *Muñoz and Garreaud* [2005] in a one-degree coastal band. We consider the alongshore momentum budget, which can be written as follows,

$$\frac{\partial V}{\partial t} = -U\frac{\partial V}{\partial x} - V\frac{\partial V}{\partial y} - W\frac{\partial V}{\partial z} - \frac{1}{\rho}\frac{\partial P}{\partial y} - fU + V_m, \quad (1)$$

where $x$, $y$, and $z$ denote the cross-shore, alongshore, and vertical directions, $U$, $V$, and $W$ are the cross-shore, alongshore, and vertical components of the near-surface wind vector, $\rho$ is the air density, $P$ is sea level pressure, $f$ is the Coriolis parameter, and $V_m$ includes vertical and horizontal diffusion. The terms represent, from left to right, the rate of change of alongshore velocity, cross-shore, alongshore, and vertical advection of alongshore momentum, alongshore pressure gradient, Coriolis force, and friction.

The alongshore budget is computed offline from the monthly mean climatological sea level pressure, air density, zonal, meridional, and vertical velocities, assuming a steady state (the left-hand side of (1) is zero) and a closed budget, i.e., the friction term is simply estimated as the residual. Trends in the alongshore wind have a negligible contribution due to long time scales ($O(10^{-10}$ m s$^{-2})$ according to Fig. 2), while advection associated with high-frequency synoptic variability not accounted for in the monthly climatological means may contribute to discrepancies between the residual and actual friction. The coastline angle is estimated at each latitude from the position of the coastline defined by the land-sea mask: the resulting angle is smoothed in order to reduce noise originating from model resolution and from the contour of the land-sea mask.

Results show that the time-averaged alongshore momentum budget is dominated by two terms, which nearly compensate each other: alongshore pressure gradient and friction (Fig. 8b). With the exception of the weak wind regions near 2–4°S, 20°S, and south of 35°S (Fig. 8a), the pressure gradient term is always positive and larger than the Coriolis and advection terms. The advection terms are generally smaller than the Coriolis term, which itself is weak due to the proximity of the Andes orographic barrier, imposing $U$~0 in the land gridpoints adjacent to the ocean. Assuming a Rayleigh friction, the balance may be seen as a quasi-linear relation between alongshore pressure gradient and alongshore velocity [*Muñoz and Garreaud*, 2005],

$$\frac{1}{\rho}\frac{\partial P}{\partial y} \approx V_m \approx -cV \,, \qquad (2)$$

with $c$>0 the friction coefficient. A quasi-linear relation between NCEP-NCAR reanalysis meridional pressure gradient (along 74°W) and QuikSCAT surface wind (at 33°S) was indeed found near the Chile coast [*Garreaud and Falvey*, 2009].

With $CO_2$ quadrupling, the alongshore pressure gradient term decreases moderately (~20%) north of ~13°S and between 23°S and 33°S, and more strongly (~40%) near 14°S–18°S (Fig. 8b). Off Peru, the friction term also decreases. South of 33°S, differences between the PI and $4CO_2$ runs become more important. The alongshore pressure gradient maximum shifts poleward from ~32°S in PI to ~35°S in $4CO_2$ (Fig. 8b), in association with the poleward shift of the SPA (Fig. 6). These results show that the change in alongshore velocity (e.g. weakening off Peru, Fig. 8a) induced by climate change is associated with a change in alongshore pressure gradient (e.g. weakening off Peru, Fig. 8b).

In the cross-shore direction, the momentum balance may be written as:

$$\frac{\partial U}{\partial t} = -U\frac{\partial U}{\partial x} - V\frac{\partial U}{\partial y} - W\frac{\partial U}{\partial z} - \frac{1}{\rho}\frac{\partial P}{\partial x} + fV + U_m, \qquad (3)$$

where $U_m$ represents friction in the cross-shore direction. According to *Garreaud and Muñoz* [2005], this balance is simpler as advection and friction are weak, which leads to an approximately geostrophic balance in the steady state,

$$\frac{1}{\rho}\frac{\partial P}{\partial x} \approx fV \qquad (4)$$

Combining (2) and (4) leads to an in-phase relation between the cross-shore and alongshore pressure gradients,

$$\frac{\partial P}{\partial x} \approx \frac{-f}{c}\frac{\partial P}{\partial y} \qquad (5)$$

Thus, this relation predicts a decrease (an increase) in the cross-shore pressure gradient off Peru (off Chile) with climate change, which is indeed found in our model solutions, although we also find that the contribution of friction in the cross-shore momentum balance is not negligible (figures not shown). Fig. 8c shows the alongshore variations of the cross-shore gradient of air temperature at 2 m height (at the ~50 km grid scale). This gradient is positive almost everywhere for PI, i. e. with higher air temperature along the coastal landmass than over the adjacent coastal ocean, except near 15°S–26°S. In the $4CO_2$ scenario, the cross-shore gradient shifts to positive values between 18°S and 28°S, and increases very strongly over most of the coastal domain (from ~50% near 8°S to ~200% near 32°S, Fig. 8c). Changes are generally half as strong in the $2CO_2$ scenario (Fig. 8c). However, this substantial increase in the coastal land-sea temperature gradient is not sufficient to generate a concurrent increase in the cross-shore pressure gradient off Peru as hypothesized by *Bakun* [1990], indicating that other processes are at least equally important in controlling the coastal wind changes.

### 3.4. Sensitivity to the chosen models and climate scenarios

To test the robustness of these results, changes in surface winds are also assessed in another configuration of the atmospheric model, LMDz-SA1, with different SST forcing, climate scenario, and experimental setup (see section 2). The summertime surface winds in the LMDz-SA1 CR are compared to their counterparts in the LMDz-ESP05 CR and to the SCOW data in Fig. 9. Most obvious from the figure is that while LMDz-ESP05 significantly overestimates the Chilean coastal jet intensity (9 m $s^{-1}$ vs. 7.5 m $s^{-1}$ in SCOW, Figs. 9b-c), LMDz-SA1 represents the coastal jet with the right amplitude but displaced ~5° to the north near 28°S–30°S (Fig. 9a), which corresponds to its wintertime position (not shown). The misplaced coastal jet in LMDz-SA1 may be explained by the location of the westerlies, which tend to be too close to the equator at lower horizontal resolutions [*Roeckner et al.*, 2006; *Arakelian and Codron*, 2012; Figs. 9a-c]. Indeed, the center of the high-pressure system and the adjacent westerly wind belt are displaced to the north in LMDz-SA1 compared to both LMDz-ESP05 and SCOW, just like the respective coastal jets. The meridional location of the westerlies likely controls the anticyclone meridional extent and thus the branch of equatorward winds near the coast, embedding the coastal jet. The offshore trade winds corresponding to the SPA northern branch are correctly reproduced by LMDz-SA1 in terms of amplitude and pattern, whereas they are too strong and meridionally narrower than observed in LMDz-ESP05 (Figs. 9a-c). On the other hand, winds off the Peru coast between the equator and 10°N are more severely underestimated in LMDz-SA1 compared to LMDz-ESP05, while they are too weak (too strong) in LMDz-SA1 (LMDz-ESP05) south of 35°S and in LMDz-ESP05 between 10°S and 25°S (Fig. 9). Unlike SCOW and to some extent, LMDz-ESP05, there is no clear drop-off zone near the coast in LMDz-SA1, where the land mask extends too far offshore as a result of the coarser horizontal resolution (Fig. 9a). Overall, LMDz-SA1 is consistent with the observed summertime regional low-level circulation and nearshore surface winds, and despite a few significant differences with LMDz-ESP05, appears equally skilled in reproducing the observation.

The LMDz-SA1 CR summertime alongshore wind and temperature cross-shore structures at 15°S and 30°S are then compared to ERA-Interim (Fig. 10). At 15°S, compared to winter (Fig. 5b), the reanalyzed winds are much weaker at all levels in summer and the maximum surface winds are located much farther offshore near 82–84°W (Fig. 10b), consistently with the SCOW data (Figs. 4c, 9c). LMDz-SA1 qualitatively reproduces the ERA-Interim wind structure (Fig. 10a). The stronger LMDz-SA1 winds, particularly in the boundary layer, are not conclusive since surface winds tend to be slightly weaker than observed in this region (Figs. 9a, 9c), which may indicate a bias in the reanalysis data. On the other hand, the temperature inversion seen in ERA-Interim data also in summer is severely underestimated in LMDz-SA1 in terms of amplitude, cross-shore extent, and vertical extent (Figs. 10a, 10b). The GCM temperature field also suffers from a cold bias of a few degrees, especially at higher levels. The weak, shallow and narrow

LMDz-SA1 temperature inversion compared to ERA-Interim and to radiosonde observations [*Garreaud et al.*, 2011] is also evident at 30°S. The coastal winds are overestimated by ~1 m $s^{-1}$ (~10.5 m $s^{-1}$ vs. ~9.5 m $s^{-1}$, Figs. 10c, 10d) as a result of the displaced coastal jet in the GCM (Fig. 9). Both wind speeds are however within the range of radiosonde observations at the same latitude (5-15 m $s^{-1}$), which are subject to significant small-scale and diurnal variability [*Garreaud et al.*, 2011]. Overall, although the vertical structure of the alongshore winds in LMDz-SA1 agrees well with the reanalysis data, the poor representation of the temperature inversion, which may partly result from lower resolution compared to LMDz-ESP05, limits to some extent the significance of warming scenarios in this GCM. In fact, it is common for both reanalyses and numerical models to have problems representing adequately the low-level atmospheric structure, particularly sharp thermal inversions [*Garreaud et al.*, 2001; *Wyant et al.*, 2010]. Note that as for LMDz-ESP05, the Andes are represented with greater detail in LMDz-SA1 than in ERA-Interim due to higher horizontal resolution, which is particularly obvious at 30°S (Fig. 10).

Compared to LMDz-ESP05, the response of the low-level circulation to global warming is strikingly different in LMDz-SA1 (Fig. 11a). The SPA does not migrate in FSSTG compared to CR. Instead, it is intensified and its poleward extent is reduced, as evidenced by anticyclonic (cyclonic) anomalous circulation north (south) of 35°S. In fact, the poleward shift and intensification of the SPA is larger in IPSL-CM4 than in the ensemble mean based on 12 CGCMs (see Fig. 1 in *Echevin et al.* [2012]), which may explain the differences found between LMDz-ESP05 and LMDz-SA1. Different SST changes in IPSL-CM4 and in the 9-model ensemble may also contribute, particularly since the former shows a stronger asymmetry in zonal-mean SST changes than the latter [*Gastineau et al.*, 2009; *Junquas et al.*, 2013]. The SST gradient between the tropics and the subtropics is known to exert a significant control on the projected poleward expansion of the Hadley circulation (and thus possibly also on the SPA), likely through changes in dry static stability. Then LMDz-ESP05, forced by IPSL-CM4 SST changes, could be more sensitive to such zonal-mean changes than LMDz-SA1. The intensification of the high-pressure system in LMDz-SA1 generates a moderate strengthening of upwelling-favorable winds (<1 m $s^{-1}$) along most of the Peru-Chile coast with a maximum in the coastal jet area located near 30°S (Fig. 9a), except north of 5°S where anomalous northerly winds induce a slight decrease in equatorward flow (<0.5 m $s^{-1}$). The summer-mean alongshore momentum balance in LMDz-SA1 CR (Fig. 11b) is very similar to the annual-mean balance in LMDz-ESP05 PI (Fig. 8b), with the alongshore pressure gradient largely compensated by friction, except South of 35°S where the Coriolis term becomes important. However, the response to $CO_2$ doubling and A1B SST increase (FSSTG scenario, red curves on Fig. 11b) is distinct in LMDz-SA1, with a slight ~20% decrease (increase) in the alongshore pressure gradient term north of 5°S–10°S (between 20°S and 35°S) and similar changes in friction. Conversely to LMDz-ESP05, there is no meridional shift in the alongshore pressure gradient maximum in LMDz-SA1 (Fig. 11b), in agreement with the stationary SPA (Fig. 11a). South of 33°S, the geostrophic balance in the alongshore direction is intensified in LMDz-SA1 with concurrent increases in the Coriolis and alongshore pressure gradient terms (Fig. 11b), while the poleward SPA migration in LMDz-ESP05 causes geostrophy to break down due to the disappearance of the alongshore pressure gradient in this region (Fig. 8b). These results confirm that changes in the alongshore wind are associated with changes in the alongshore pressure gradient also in LMDz-SA1. In both models, these are clearly related off central Chile to changes in the SPA position and/or intensity, whereas the origin of opposite changes off Peru are less clear.

### 3.5. Vorticity budget and precipitation/wind/SST feedbacks off Peru

Winds off the coast of Peru may be too far from the SPA to be significantly affected by its intensification, although they might be affected by its poleward shift and the related alongshore pressure gradient decrease, inducing a weakening in upwelling-favorable winds and Ekman suction. This may be one reason why the wind reduction off Peru is weaker and confined to the north in the LMDz-SA1 model compared to the LMDz-ESP05 model, since the SPA expands southward only in the latter. However, this may not be the whole story. If alongshore wind changes off Peru were solely driven by changes in the SPA characteristics, there would likely be relatively little dispersion in the responses simulated by CMIP3 CGCMs, as is the case off Chile (Fig. 2), the SPA migration being a relatively consistent feature among the models [*Garreaud and Falvey*, 2009]. This is not the case, especially in austral winter when the SPA is located in its northernmost position (Fig. 2). Another possibility is related to the existence of precipitation/wind/SST feedbacks in the tropics.

CMIP3 CGCMs have strong positive biases in precipitation and SST off Peru (typically 2 mm/day and 3°C [*Christensen et al.*, 2007]), simulating a warm, moist, "tropical" climate regime with spurious convective rainfall in a region that in nature is characterized by large-scale subsidence, cool ocean temperatures, and a coastal desert. With $CO_2$ quadrupling, many of these models including IPSL-CM4 project an increase in precipitation off northern Peru where surface warming is stronger, associated with a slowdown in southeasterly winds (i.e., northwesterly anomalies, Fig. 12). This tendency is particularly marked in summer when SSTs are warmer and the ITCZ is located at its southernmost position in the tropical eastern North Pacific (not shown).

The increase in rainfall may be the result of increased moisture content and transport in the atmosphere [*Held and Soden*, 2006] or of a reduction in static stability associated with relatively strong surface warming in the $4CO_2$ scenario. It is likely associated with an increase in convection and cloud formation in the presence of warmer than observed SST in the CGCMs.

The CGCM tendency toward reduced winds and increased precipitation off northern Peru (Fig. 12) is qualitatively reproduced in LMDz-ESP05 in summer, with a strong increase in rainfall (1–2 mm/day or more) off central and northern Peru north of 10°S–15°S (Fig. 13a). Changes in rainfall are weak elsewhere and in winter (Fig. 13b). In LMDz-SA1, rainfall also increases significantly in summer by 0.5–1 mm/day near 5°S–10°S [*Junquas et al.*, 2013; their Fig. 8b]. This region is located just south of northerly wind anomalies and is characterized by anomalous surface wind convergence in the model (Fig. 11a). Note that LMDz-SA1 has almost no bias in precipitation over the ocean in the PCUS compared to observed climatologies [*Junquas et al.*, 2013; their Fig. 4c], while biases in the LMDz-ESP05 CR are much weaker than in CGCM 20C3M simulations (not shown).

The analysis of the steady-state vorticity balance on the *β*-plane can help understanding the dynamical relationship between alongshore wind and vertical motion, which in turn can be associated with moist convection [e. g. *Kodama*, 1999] and subsidence [e. g. *Takahashi and Battisti*, 2007b]. For simplicity, consider the case of a purely meridional eastern boundary. Equations (1) and (3) then become the meridional and zonal momentum budgets, respectively. We then subtract the meridional derivative of (3) from the zonal derivative of (1) to derive a vorticity balance:

$$\frac{\partial \xi}{\partial t} = -\xi \frac{\partial U}{\partial x} - U \frac{\partial \xi}{\partial x} - \xi \frac{\partial V}{\partial y} - V \frac{\partial \xi}{\partial y} + \frac{\partial W}{\partial y} \frac{\partial U}{\partial z} - \frac{\partial W}{\partial x} \frac{\partial V}{\partial z} - W \frac{\partial \xi}{\partial z}$$

$$-\beta V - f\left(\frac{\partial U}{\partial x}+\frac{\partial V}{\partial y}\right)+\frac{\partial V_m}{\partial x}-\frac{\partial U_m}{\partial y}, \tag{6}$$

where $\xi = \partial V/\partial x - \partial U/\partial y$ is relative vorticity and $\beta$ is the meridional gradient of the Coriolis parameter *f*. At steady state $(\partial\xi/\partial t \approx 0)$, using the continuity equation $-(\partial U/\partial x + \partial V/\partial y) = \partial W/\partial z$ that relates surface wind convergence to convection, we obtain the vorticity balance

$$\beta V \approx -\left(\xi\frac{\partial U}{\partial x}+U\frac{\partial \xi}{\partial x}+\xi\frac{\partial V}{\partial y}+V\frac{\partial \xi}{\partial y}-\frac{\partial W}{\partial y}\frac{\partial U}{\partial z}+\frac{\partial W}{\partial x}\frac{\partial V}{\partial z}+W\frac{\partial \xi}{\partial z}\right)+f\frac{\partial W}{\partial z}+\left(\frac{\partial V_m}{\partial x}-\frac{\partial U_m}{\partial y}\right)$$

(7)

Equation (7) states that planetary vorticity (term on the left-hand side) is balanced by the sum of the curl of advection (seven terms in brackets on the right-hand side), vortex stretching (proportional to $\partial W/\partial z$, *i.e.* to convection/subsidence), and the curl of friction (two terms in brackets on the right-hand side). From the previous analysis of the momentum bugets, it is suspected that the advection term has a weak contribution to the vorticity balance, which is indeed verified (see below). Hence, in regions where changes in the frictional term are small, a decrease (increase) in planetary vorticity and thus in equatorward alongshore wind is then associated with anomalous upward (downward) motion.

Similarly to the momentum balances, the vorticity balance is computed from the monthly mean climatological LMDz-ESP05 outputs and from the DJF seasonal mean LMDz-SA1 outputs. The residuals of the meridional and zonal momentum balances are used to estimate the curl of friction. Fig. 14 shows the vorticity balance and its change in the climate scenarios for the two GCMs off Peru in summer when the rainfall anomalies occur (Fig. 13a). In both cases, the balance was found to be approximately closed with a negligible residual (not shown). Note that successive differenciations used to derive the momentum and vorticity budgets introduce a low signal-to-noise ratio near the coast, where cross-shore gradients in surface winds and sea level pressure are large due to the presence of the Andes. Therefore, the analysis is not appropriate for the nearshore region, but is suitable to infer the dynamics of wind changes in the offshore region where precipitation anomalies are found (Fig. 13a).

In both GCMs, the balances are similar, with planetary vorticity balanced by the sum of vortex stretching and the curl of friction (white contours on Fig. 14). The contribution of the curl of advection is found to be weak compared to the other terms (Figs. 14d, 14h), which confirms our hypothesis. The friction term dominates in the regions where convection occurs ($f\,\partial W/\partial z < 0$) in the LMDz-ESP05 PI (near 5°S–10°S, Figs. 14b-c) and LMDz-SA1 CR (near 5°S–15°S, Figs. 14f-g) simulations. The opposite tends to take place further south with planetary vorticity and vortex stretching in approximate balance.

With $CO_2$ quadrupling, a strong negative anomaly of vortex stretching near 5°S–14°S (shading on Fig. 14b) is associated with an increase in precipitation (Fig. 13a). This anomaly is only partially equilibrated by a concurrent increase in the friction term (Fig. 14c) because it is itself mostly compensated by a negative anomaly in the advection term (Fig. 14d). Therefore, the northwesterly wind anomaly in the region of precipitation increase (and convective anomaly) between PI and $4CO_2$ (Fig. 13a) may be interpreted dynamically as the result of approximately balanced reductions in vortex stretching and planetary vorticity with global warming (Figs. 14a-b). In LMDz-SA1, only a weak negative anomaly of vortex stretching appears near 5°S–10°S (Fig. 14f) and is compensated by the curls of friction (Fig. 14g) and advection (Fig. 14h), leading to weak wind changes in this region (Fig. 14a) despite the increase in rainfall [Fig. 8b by *Junquas et al.*, 2013]. Such differences between the convective anomalies in the two GCMs may be related to the much stronger (twice or more) rainfall increase in LMDz-ESP05 compared to LMDz-SA1. It was checked that similar results were obtained in LMDz-ESP05 with $CO_2$ doubling but with weaker changes, consistent with the quasi-linear response to greenhouse gas increase found throughout this paper.

In contrast, in the equatorial region (0°N–5°S), the reduction in planetary vorticity rather appears to be associated with a reduction in the curl of friction, both in LMDz-ESP05 and LMDz-SA1 (Figs. 14a, 14c, 14e, 14g), suggesting the same process is taking place in the two GCMs. Both vortex stretching and its change are weak in this region (Figs. 14b, 14f), partly because the Coriolis parameter vanishes at the equator. These results suggest that equatorial and off-equatorial wind changes are driven by different dynamics and that wind/precipitation feedbacks only play a role away from the equator. This provides a possible explanation for the differences in wind and rainfall changes in LMDz-ESP05 and LMDz-SA1. Note that the patch of rainfall increase near the equator in LMDz-ESP05 (Fig. 13a) is not associated with a convective anomaly (Fig. 14b), suggesting it may result from southward anomalous moisture transport from the ITCZ north of the equator.

## 4. Discussion and conclusions

Regional dynamical downscaling using the LMDz GCM was performed in the Peru-Chile upwelling system to study changes in alongshore surface wind and wind stress curl over the ocean due to global warming. Three idealized climate scenarios (with constant preindustrial, doubled, and quadrupled $CO_2$ concentrations in the atmosphere) from the IPSL-CM4 CGCM were downscaled to examine the surface wind changes and the physical mechanisms at stake. Our results show a weakening of upwelling-favorable winds and Ekman suction off Peru and northern Chile, and an intensification off central Chile, with a quasi-linear response to $CO_2$ increase. The robustness of these projections was assessed by comparing with a different configuration of the LMDz GCM run under other climate scenarios (20th century climate and A1B scenario with doubled $CO_2$ concentrations) and CGCM SST forcing (multimodel ensemble mean), in which case reduced winds were only found off northern Peru with intensified winds elsewhere. While quantitatively different, the results from this sensitivity experiment suggest that opposed wind projections, with a weakening off Peru and a strengthening off Chile, may be robust features in the climate scenarios.

Consistently with previous studies, the presence of the Andes precludes the establishment of the geostrophic equilibrium in the alongshore direction, imposing a balance between the alongshore pressure gradient and friction in both GCMs [*Muñoz and Garreaud*, 2005; *Garreaud and Falvey*, 2009]. In the Chile region, the increase in coastal winds is thus likely due to a poleward displacement and/or an intensification of the maximum alongshore pressure gradient (Figs. 8b, 11b) due to similar changes in the South Pacific anticyclone (SPA; Figs. 6, 11a) and Hadley circulation [e.g., *Lu et al.*, 2007; *Previdi and Liepert*, 2007]. Further north off Peru, the reduction in coastal winds and Ekman suction may be related either to the SPA southward shift and the associated reduction in the alongshore pressure gradient, or to summertime anomalous upward motion and associated negative vortex stretching anomaly in both the global CMIP3 models and the higher-resolution LMDz-ESP05 GCM. Although the dynamical relation (7) does not indicate causality, changes in vertical velocity might be associated with changes in convective precipitation, so the summertime wind reduction off Peru in LMDz-ESP05 could be a result of enhanced convection and rainfall due to the warming of the ocean surface and associated decrease in static stability. In addition to the direct greenhouse gas forcing, the ocean warming could also be forced through the equatorial Pacific dynamical response to future global warming, which includes a weakening of the Walker circulation and a flattening of the thermocline [*Vecchi and Soden*, 2007]. The resulting weakening of the wind could provide a positive feedback that would amplify the initial response. However, given the strong biases in present-climate rainfall and SST off Peru in the CGCMs, the relevance of the projected precipitation/SST changes to the real climate is not clear yet. Other forcing and feedback processes involving low-level clouds may also be contributing to the changes in precipitation, SST and winds, but their analysis is beyond the scope of this paper.

These results also raise an important point: how do we reconcile the climate-change wind decrease with the enhanced trade winds during El Niño events, both near the coast and at the large scale [*Wyrkti*, 1975; *Enfield*, 1981; *Huyer et al.*, 1987; *Halpern*, 2002]? This increase could be explained by an enhancement of the land-sea thermal contrast due to changes in coastal cloudiness [*Enfield*, 1981], but perhaps more likely by the enhanced alongshore thermal gradient associated with maximum warming off northern Peru, as suggested by in-phase relation between the changes in alongshore wind and SST gradients (e.g. Fig. 9 by *Rasmusson and Carpenter* [1982]), as well as by atmospheric model experiments [*Quijano-Vargas*, 2011]. The alongshore SST gradient anomalies in climate-change simulations (Fig. 12) appear to be substantially weaker than during the observed El Niño, so the wind response should also be expected to be weaker. On the other hand, northerly wind anomalies have also been observed during El Niño, but to the north of the maximum warming [*Rasmusson and Carpenter*, 1982]. This was more dramatic during the 1925-1926 El Niño, when strong northerlies and the ITCZ invaded the southern hemisphere [Takahashi, K., A. G. Martínez, and K. Mosquera-Vásquez, The very strong 1925-26 El Niño in the far eastern Pacific, revisited, *Clim. Dyn.*, in prep.]. A situation like the latter is unrealistically common in coupled GCMs, likely a reflection of their large biases in this region.

We now discuss the limits of our approach. A first limitation is the use of a single GCM, LMDz, which limits the robustness of our findings. However, results show that LMDz is able to reproduce distinct processes leading to opposite wind changes off the coast of Peru, depending on SST forcing and model configuration. Using distinct CGCM, scenario, and atmospheric model, *Garreaud and Falvey* [2009] found a fall-winter wind increase of 0.4–0.8 m $s^{-1}$ in the core of the Chilean coastal jet (near 25°S–35°S), which is close to the wind change (0.5–1 m $s^{-1}$) in the coastal jet core (near 30°S–37°S) in both LMDz-ESP05 and LMDz-SA1. Our results are also in line with previous findings obtained from statistical downscaling of the same IPSL-CM4 scenarios [*Goubanova et al.*, 2011]. In their study, wind changes off Peru and northern Chile were moderate, with a maximum decrease of ~5% ($2CO_2$) to ~10% ($4CO_2$) off Peru in summer and almost no change during winter. Similarly to our study, the largest increase occurred in summer south of 35°S and reached ~10% in $2CO_2$ and 10–20% in $4CO_2$, respectively. The main discrepancy between our results and theirs is the stronger decrease off central Chile (10–20%) and central Peru (20–30%) in summer in our simulations. They thus corroborate the assumption of persistence of model-data statistical relations with climate change that was made as part of the statistical downscaling procedure. Using the statistical downscaling method of *Goubanova et al.* [2011], *Goubanova and Ruiz* [2010] studied an ensemble of 12 CGCMs under the SRES A2 scenario [*Nakicenovic et al.*, 2000]. They found a moderate ensemble-mean wind increase (less than 0.3 m $s^{-1}$) during winter and a weak decrease (less than 0.2 m $s^{-1}$) in summer off Peru. Off Chile, the wind increases substantially (0.4–0.6 m $s^{-1}$ near 24°S–32°S) during winter and the increase is weaker (0.1–0.2 m $s^{-1}$) during summer. Further south near 35°S–40°S, the wind increases strongly all year round, peaking (~0.9 m $s^{-1}$) in March-April and in September-November. Hence, although different climate scenarios were analyzed here, results from both studies are consistent with our projections for the Chile region. The *Goubanova and Ruiz* [2010] study that included the Peru region also found reduced summertime winds there, which gives us confidence in the projected changes off Peru.

These modelling results, like those of *Goubanova et al.* [2011] and *Goubanova and Ruiz* [2010], are consistent with the trends in upwelling-favorable winds observed in the last decades using adjusted ship-based measurements from the Wave and Anemometer-based Sea-surface Wind (WASWind) [*Tokinaga and Xie*, 2011] to correct for spurious positive trends due to an increase in anemometer height [*Cardone et al.*, 1990]. Indeed, WASWind data shows little signal off Peru but an increase off central Chile (Fig. 1), significantly smaller and even reversed relative to the initial estimations by *Bakun* [1990]. Although *Bakun* [1990]'s argument that an increased cross-shore temperature gradient due to increased warming over land drives an increased equatorward wind may hold for several eastern boundary upwelling systems [*Falvey and Garreaud*, 2009; *Snyder et al.*, 2002; *Miranda et al.*, 2012], it is not clear whether it is important in the Peru region.

Indeed, such mechanism requires the intensification of a thermal low-pressure cell over land – and thus of the cross-shore pressure gradient – driving an intensification of equatorward geostrophic wind [*Bakun*, 1990]. In the model results presented here, the intensified cross-shore temperature gradient is associated with a reduction in the cross-shore pressure gradient off Peru and a weakening of alongshore winds. An increased land-sea thermal gradient may thus not necessarily lead to a wind increase in the Peru region. This will have to be verified using other models with a higher spatial resolution. Note that the recent analysis of observed wind and SST trends suggests that similarly to Peru, the Iberian and North African eastern boundary upwelling systems show no significant increase in upwelling-favorable winds and even a warming of the coastal zone [*Barton et al.*, 2013], in disagreement with *Bakun* [1990]'s hypothesis.

A potential limitation of our study is the relatively modest spatial resolutions attained in the LMDz-ESP05 and LMDz-SA1 zooms (~50 km and ~100 km, respectively). Although the relatively low vertical resolution (19 levels) could have an effect on the simulation near the surface, *Wyant et al.* [2010] did not find any clear relationship between vertical resolution and model skill in simulating the boundary layer structure. Small-scale effects, such as those associated with coastal capes [*Boé et al.*, 2011], sea breeze [*Franchito et al.*, 1998], intensified temperature gradient induced by the warming of the narrow desertic plains located between the coast and the high Andes off Peru and northern Chile (~ 1-2 grid points in our models) could also have an effect. Yet, using the MM5 regional climate model [*Grell et al.*, 1994] in the central Peru coastal jet region at higher horizontal resolutions than in our models (45 km, 15 km, and 5 km), *Quijano-Vargas* [2011] found that friction equilibrated the alongshore pressure gradient, in agreement with *Muñoz and Garreaud* [2005] and this study. He however found that for mesoscale features, the advection of momentum contributed significantly to the balance in some specific areas of the coastal jet region.

Another limitation of our study is the absence of two-way feedback between the ocean and the atmosphere in our regional, SST-forced experiments. The SST fields forcing the GCM are composed of a medium-scale climatology (AMIP, ~1°) and a large-scale SST anomaly from the CGCM (~2°). While the climatological field partly represents the upwelling mesoscale cross-shore SST gradient, the spatial scales of the SST anomalies are larger and cross-shore gradients could be underestimated. Regional ocean simulations forced by the LMDz-ESP05 CR wind stress fields show that small-scale cross-shore SST gradients are larger (~$2.10^{-5}$ °C $m^{-1}$) near the Peru coast [Oerder, V., F. Colas, V. Echevin, F. Codron, J. Tam, and A. Belmadani, Peru-Chile upwelling dynamics under climate change, *Clim. Dyn.*, in prep.] than in AMIP SST fields (<$10^{-5}$ °C $m^{-1}$, not shown). Mesoscale variations in SST may induce variations in the surface wind [*Chelton et al.*, 2007; *Small et al.*, 2008; *Boé et al.*, 2011; *Perlin et al.*, 2011*; Renault et al.*, 2012] with a potentially strong impact on the upwelling dynamics (*e.g.*, *Jin et al.* [2009]). Clearly, a regional ocean-land-atmosphere coupled model is needed to investigate such processes and assess their impact on coastal winds, upwelling and the marine ecosystem.

**Acknowledgements**

The LMDz-ESP05 simulations were performed on Brodie, the NEC SX8 computer at Institut du Développement et des Ressources en Informatique Scientifique (IDRIS), Orsay, France. The LMDz-SA1 simulations were performed on Calcul Intensif pour le Climat, l'Atmosphère et la Dynamique (CICLAD), a PC cluster at IPSL, within the framework of previous research supported by the European Commission's Seventh Framework Programme (FP7/2007-2013) under Grant Agreement N°212492 (CLARIS LPB. A Europe-South America Network for Climate Change Assessment and Impact Studies in La Plata Basin), CNRS/LEFE Program, and CONICET PIP 112-200801-00399. A. Belmadani was supported by the Agence Nationale de la Recherche (ANR) Peru Ecosystem Projection Scenarios (PEPS, ANR-08-RISK-012) project. Additional support was provided by the Japan Agency for Marine-Earth Science and Technology (JAMSTEC), by the National Aeronautics and Space Administration (NASA) through grant NNX07AG53G, and by the National Oceanic and Atmospheric Administration (NOAA) through grant NA11NMF4320128, which sponsor research at the IPRC. A. Belmadani is now supported by the Universidad de Concepcion (UdeC). V. Echevin and C. Junquas are supported by the Institut de Recherche pour le Développement (IRD). F. Codron is supported by the Université Pierre et Marie Curie (UPMC). K. Takahashi is supported by the Instituto Geofisico del Peru (IGP). K. Hamilton, A. Lauer, and Y. Wang are thanked for fruitful discussions. This is the IPRC/SOEST publication #XXXX/YYYY.

**References**

Albert, A., V. Echevin, M. Lévy, and O. Aumont (2010), Impact of nearshore wind stress curl on coastal circulation and primary productivity in the Peru upwelling system, *J. Geophys. Res.*, *115*, C12033, doi:10.1029/2010JC006569.

Arakelian, A., and F. Codron (2012), Southern hemisphere jet variability in the IPSL GCM at varying resolutions, *J. Atmos. Sci.*, *56*, 4032–4048.

Bakun, A. (1990), Global climate change and intensification of coastal upwelling, *Science*, *247*, 198–201, doi:10.1126/science.247.4939.198.

Bakun, A., and S. J. Weeks (2008), The marine ecosystem off Peru: What are the secrets of its fishery productivity and what might its future hold?, *Prog. Oceanogr.*, *79*, 290–299, doi:10.1016/j.pocean.2008.10.027.

Bakun, A., D. Field, A. Renondo-Rodriguez, and S. J. Weeks (2010), Greenhouse gas, upwelling favourable winds, and the future of upwelling systems, *Global Change Biol.*, *16*, 1,213–1,228, doi:10.1111/j.1365-2486.2009.02094.x.

Barton, E. D., D. B. Field, and C. Roy (2013), Canary current upwelling: More or less?, *Prog. Oceanogr.*, doi:10.1016/j.pocean.2013.07.007, in press.

Belmadani, A., B. Dewitte, and S.-I. An (2010), ENSO feedbacks and associated time scales of variability in a multimodel ensemble, *J. Clim.*, *23*, 3,181–3,204, doi:10.1175/2010JCLI2830.1.

Boé, J., A. Hall, F. Colas, J. C. McWilliams, X. Qu, J. Kurian, and S. B. Kapnick (2011), What shapes mesoscale wind anomalies in coastal upwelling zones?, *Clim. Dyn.*, *36*(11-12), 2037-2049, doi:10.1007/s00382-011-1058-5.

Boville, B. A., and P. R. Gent (1998), The NCAR climate system model, version one, *J. Clim.*, *11*, 1,115–1,130, doi:10.1175/1520-0442(1998)011<1115:TNCSMV>2.0.CO:2.

Capet, X. J., P. Marchesiello, and J. C. McWilliams (2004), Upwelling response to coastal wind profiles, *Geophys. Res. Lett.*, *31*, L13311, doi:10.1029/2004GL020123.

Cardone, V. J., J. G. Greenwood, and M. A. Cane (1990), On trends in historical marine wind data, *J. Clim.*, *3*, 113–127, doi:10.1175/1520-0442(1990)003%3C0113%3AOTIHMW%3E2.0.CO%3B2.

Chavez, F. P. (1995), A comparison of ship and satellite chlorophyll from California and Peru, *J. Geophys. Res.*, *100*, 24,855–24,862, doi:10.1029/95JC02738.

Chavez, F. P., A. Bertrand, R. Guevara-Carrasco, P. Soler, and J. Csirke (2008), The northern Humboldt Current System: Brief history, present status and a view towards the future, *Prog. Oceanogr.*, *79*, 95–105, doi:10.1016/j.pocean.2008.10.012.

Chelton, D. B., M. G. Schlax, and R. M. Samelson (2007), Summertime coupling between sea surface temperature and wind stress in the California Current System, *J. Phys. Oceanogr.*, 37, 495–517.

Chen, W., Z. Jiang, L. Li, and P. Yiou (2011), Simulation of regional climate change under the IPCC A2 scenario in southeast China, *Clim. Dyn.*, *36*, 491–507.

Christensen, J. H., et al. (2007), Regional Climate Projections, in *Climate Change 2007: The Physical Science Basis, Contribution of Working Group I to the Fourth Assessment Report of the Intergovernmental Panel on Climate Change*, edited by S. Solomon, D. Qin, M. Manning, Z. Chen, M. Marquis, K. B. Averyt, M. Tignor and H. L. Miller, Cambridge University Press, Cambridge, United Kingdom and New York, NY, USA.

Dee, D. P., et al. (2011), The ERA-Interim reanalysis: Configuration and performance of the data assimilation system, *Quart. J. Roy. Met. Soc., A, 137*, 553–597, doi:10.1002/qj.828.

Demarcq, H. (2009), Trends in primary production, sea surface temperature and wind in upwelling systems (1998–2007), *Prog. Oceanogr.*, *83*, 376–385, doi:10.1016/j.pocean.2009.07.022.

Echevin, V., K. Goubanova, A. Belmadani, and B. Dewitte (2012), Sensitivity of the Humboldt Current system to global warming: A downscaling experiment of the IPSL-CM4 model, *Clim. Dyn.*, *38*, 3–4, 761–774, doi:10.1007/s00382-011-1085-2.

Enfield, D. B. (1981), Thermally-driven wind variability in the planetary boundary layer above Lima, Peru, *J. Geophys. Res.*, *86*(C3), 2005–2016, doi:10.1029/JC086iC03p02005.

Falvey, M., and R. Garreaud (2009), Regional cooling in a warming world: Recent temperature trends in the southeast Pacific and along the west coast of subtropical South America (1979–2006), *J. Geophys. Res.*, *114*, D04102, doi:10.1029/2008JD010519.

Food and Agriculture Organization (2010), *The state of world fisheries and aquaculture 2010*, 218 pp., Fish. and Aquacult. Dep., Rome.

Franchito, S. H., V. B. Rao, J. L. Stech, and J. A. Lorenzzetti (1998), The effect of coastal upwelling on the sea-breeze circulation at Cabo Frio, Brazil: A numerical experiment, *Annales Geophysicae*, *16*(7), 866–881.

Fréon, P., M. Barange, and J. Aristegui (2009), Eastern Boundary Upwelling Ecosystems: Integrative and comparative approaches, *Prog. Oceanogr.*, *83*, 1–14.

Garreaud, R., and M. Falvey (2009), The coastal winds off western subtropical South America in future climate scenarios, *Int. J. Climatol.*, *29*, 4, 543–554, doi:10.1002/joc.1716.

Garreaud, R. D., and R. C. Muñoz (2005), The low-level jet off the west coast of subtropical South America: Structure and variability, *Mon. Wea. Rev.*, *133*, 2,246–2,261, doi:10.1175/MWR2972.1.

Garreaud, R. D., J. Rutllant, J. Quintana, J. Carrasco, and P. Minnis (2001), CIMAR-5: A snapshot of the lower troposphere over the subtropical southeast Pacific, *Bull. Amer. Meteor. Soc.*, *82*(10), 2,193–2,207.

Garreaud, R. D., J. A. Rutllant, R. C. Muñoz, D. A. Rahn, M. Ramos, and D. Figueroa (2011), VOCALS-CUpEx: the Chilean Upwelling Experiment, *Atmos. Chem. Phys.*, *11*, 2,015–2,029, doi:10.5194/acp-11-2015-2011.

Gastineau, G., H. Le Treut, and L. Li (2008), Hadley circulation changes under global warming conditions indicated by coupled climate models, *Tellus*, *60A*, 863–884, doi:10.1111/j.1600-0870.2008.00344.x.

Gastineau, G., L. Li, and H. Le Treut (2009), The Hadley and Walker circulation changes in global warming conditions described by idealized atmospheric simulations, *J. Clim.*, *22*, 3,993–4,013, doi:10.1175/2009JCLI2794.1.

Gordon, C., et al. (2000), The simulation of SST, sea ice extents and ocean heat transports in a version of the Hadley Centre coupled model without flux adjustments, *Clim. Dyn.*, *16*, 147–168, doi:10.1007/s00382-005-0010.

Goubanova, K., and C. Ruiz (2010), Impact of climate change on wind-driven upwelling off the coasts of Peru-Chile in a multi-model ensemble, in *Climate variability in the tropical Pacific: Mechanisms, modelling and observations*, edited by Y. duPenhoat and A. V. Kislov, 194–201, Maks-Press, Moscow, Russia.

Goubanova, K., V. Echevin, B. Dewitte, F. Codron, K. Takahashi, P. Terray, and M. Vrac (2011), Statistical downscaling of sea-surface wind over the Peru-Chile upwelling region: Diagnosing the impact of climate change from the IPSL-CM4 model, *Clim. Dyn.*, *36*, 7–8, 1,365–1,378, doi:10.1007/s00382-010-0824-0.

Grell, G. A., J. Dudhia, and D. R. Stauffer (1994), A description of the fifth-generation Penn State/NCAR Mesoscale Model (MM5), Tech. Note TN-398+IA, National Center for Atmospheric Research, Boulder, CO, 125 pp.

Gutiérrez, D., I. Bouloubassi, A. Sifeddine, S. Purca, K. Goubanova, M. Graco, D. Field, L. Mejanelle, F. Velazco, A. Lorre, R. Salvatteci, D. Quispe, G. Vargas, B. Dewitte, and L. Ortlieb (2011), Coastal cooling and increased productivity in the main upwelling zone off Peru since the mid-twentieth century, *Geophys. Res. Lett.*, *38*, L07603, doi:10.1029/2010GL046324.

Halpern, D. (2002), Offshore Ekman transport and Ekman pumping off Peru during the 1997–1998 El Niño, *Geophys. Res. Lett.*, *29*, 1075, doi:10.1029/2001GL014097.

Haraguchi, P. Y. (1968), Inversions over the tropical eastern Pacific ocean, *Mon. Wea. Rev.*, *96*, 177–185.

Held, I. M., and B. J. Soden (2006), Robust responses of the hydrological cycle to global warming, *J. Clim.*, *19*, 5,686–5,699, doi:10.1175/JCLI3990.1.

Hourdin, F., et al. (2006), The LMDZ4 general circulation model: Climate performance and sensitivity to parametrized physics with emphasis on tropical convection, *Clim. Dyn.*, *27*, 7–8, 787–813, doi:10.1007/s00382-006-0158-0.

Hurrell, J. W., J. J. Hack, D. Shea, J. M. Caron, and J. Rosinski (2008), A new sea surface temperature and sea ice boundary dataset for the Community Atmosphere Model, *J. Clim.*, *21*, 5,145–5,153, doi:10.1175/2008JCLI2292.1.

Huyer, A., R. L. Smith, and T. Paluszkiewicz (1987), Coastal upwelling off Peru during normal and El Niño times, 1981–1984, *J. Geophys. Res.*, *92*(C13), 14297–14307, doi:10.1029/JC092iC13p14297.

Jin, X., C. Dong, J. Kurian, J. C. McWilliams, D. B. Chelton, and Z. Li (2009), SST-wind interaction in coastal upwelling: Oceanic simulation with empirical coupling, *J. Phys. Oceanogr.*, *39*(11), 2957–2970.

Johanson, C. M., and Q. Fu (2009), Hadley cell widening: Model simulations versus observations, *J. Clim.*, *22*, 2,713–2,725, doi:10.1175/2008JCLI2620.1.

Jones, R. G., M. Noguer, D. C. Hassell, D. Hudson, S. S. Wilson, G. J. Jenkins, and J. F. B. Mitchell (2004), *Generating high resolution climate change scenarios using PRECIS*, 40 pp., Met. Office Hadley Centre, Exeter.

Junquas, C., C. Vera, L. Li, and H. Le Treut (2012), Summer precipitation variability over southeastern South America in a global warming scenario, *Clim. Dyn.*, *38*, 1867–1883.

Junquas, C., C. S. Vera, L. Li, and H. Le Treut (2013), Impact of projected SST changes on summer rainfall in southeastern South America, *Clim. Dyn.*, *40*, 7–8, 1569–1589, doi:10.1007/s00382-013-1695-y.

Kodama, Y.-M. (1999), Roles of the atmospheric heat sources in maintaining the Subtropical Convergence Zones: An aqua-planet GCM study, *J. Atmos. Sci.*, *56*, 4032–4048.

Large, W. G., and G. Danabasoglu (2006), Attribution and impacts of upper ocean biases in CCSM3, *J. Clim.*, *19*, 2,325–2,346, doi:10.1175/JCLI3740.1.

Lorenz, P., and D. Jacob (2005), Influence of regional scale information on the global circulation: A two-way nesting climate simulation, *Geophys. Res. Lett.*, *32*, L18706, doi:10.1029/2005GL023351.

Lu, J., G. A. Vecchi, and T. Reichler (2007), Expansion of the Hadley cell under global warming, *Geophys. Res. Lett.*, *34*, L06805, doi:10.1029/2006GL028443.

Marti, O., et al. (2010), Key features of the IPSL ocean atmosphere model and its sensitivity to atmospheric resolution, *Clim. Dyn.*, *34*, 1, 1–26, doi:10.1007/s00382-009-0640-6.

Miranda, P. M. A., J. M. R. Alves, and N. Serra (2012), Climate change and upwelling: Response of Iberian upwelling to atmospheric forcing in a regional climate scenario, *Clim. Dyn.*, doi:10.1007/s00382-012-1442-9.

Mitas, C. M., and A. Clement (2005), Has the Hadley cell been strengthening in recent decades?, *Geophys. Res. Lett.*, *32*, L03809, doi:10.1029/2004GL021765.

Muñoz, R. C., and R. D. Garreaud (2005), Dynamics of the low-level jet off the west coast of subtropical South America, *Mon. Wea. Rev.*, *133*, 3,661–3,677, doi:10.1175/MWR3074.1.

Nakicenovic, N., et al. (2000), *Special report on emissions scenarios: A special report of working group III of the intergovernmental panel on climate change*, 599 pp., Cambridge University Press, Cambridge.

Nigam, S. (1997), The annual warm to cold phase transition in the eastern equatorial Pacific: Diagnosis of the role of stratus cloud-top cooling, *J. Clim.*, *10*, 2447–2467.

Perlin, N., E. D. Skyllingstad, and R. M. Samelson (2011), Coastal atmospheric circulation around an idealized cape during wind-driven upwelling studied from a coupled ocean-atmosphere model, *Mon. Wea. Rev.*, *139*, 809–829.

Philander, S. G. H., D. Gu, G. Lambert, N. C. Lau, and R. C. Pacanowski (1996), Why the ITCZ is mostly north of the equator, *J. Clim.*, *9*, 2958–2972.

Pope, V., M. L. Gallani, P. R. Rowntree, and R. A. Stratton (2000), The impact of new physical parameterizations in the Hadley centre climate model: HadAM3, *Clim. Dyn.*, *16*, 123–146, doi:10.1007/s00382-005-0009.

Previdi, M., and B. G. Liepert (2007), Annular modes and Hadley cell expansion under global warming, *Geophys. Res. Lett.*, *34*, L22701, doi:10.1029/2007GL031243.

Quijano-Vargas, J. J. (2011), Simulacion de la dinamica del viento superficial sobre la costa de Ica utilizando el modelo numerico de la atmosfera de mesoescala MM5, Tesis de Maestria, 172 p.p., http://www.met.igp.gob.pe/publicaciones/2011/JQuijano_tesisUNMSM.pdf.

Rahn, D. A., and R. Garreaud (2010), Marine boundary layer over the subtropical southeast Pacific during VOCALS-Rex – Part 1: Mean structure and diurnal cycle, *Atmos. Chem. Phys.*, *10*, 4,491–4,506, doi:10.5194/acp-10-4491-2010.

Rasmusson, E. M., and T. H. Carpenter (1982), Variations in tropical sea surface temperature and surface wind fields associated with the Southern Oscillation/El Niño, *Mon. Wea. Rev.*, *110*, 354–384.

Renault, L., B. Dewitte, M. Falvey, R. Garreaud, V. Echevin, and F. Bonjean (2009), Impact of atmospheric coastal jet off central Chile on sea surface temperature from satellite observations (2000–2007), *J. Geophys. Res.*, *114*, C08006, doi:10.1029/2008JC005083.

Renault, L., B. Dewitte, P. Marchesiello, S. Illig, V. Echevin, G. Cambon, M. Ramos, O. Astudillo, P. Minnis, and J. K. Ayers (2012), Upwelling response to atmospheric coastal jets off central Chile: A modeling study of the October 2000 event, *J. Geophys. Res.*, *117*, C02030, doi:10.1029/2011JC007446.

Risien, C. M., and D. B. Chelton (2008), A global climatology of surface wind and wind stress fields from eight years of QuikSCAT scatterometer data, *J. Phys. Oceanogr.*, *38*, 2,379–2,413, doi:10.1175/2008JPO3881.1.

Roeckner, E., R. Brokopf, M. Esch, M. Giorgetta, S. Hagemann, L. Kornblueh, E. Manzini, U. Schlese, and U. Schulzweida (2006), Sensitivity of simulated climate to horizontal and vertical resolution in the ECHAM5 atmosphere model, *J. Clim.*, *19*, 3,771–3,791, doi:10.1175/JCLI3824.1.

Sepulchre, P., L. C. Sloan, M. Snyder, and J. Fiechter (2009), Impacts of Andean uplift on the Humboldt Current system: A climate model sensitivity study, *Paleoceanogr.*, *24*, PA4215, doi:10.1029/2008PA001668.

Small, J., S. P. DeSzoeke, S.-P. Xie, L. O'Neill, H. Seo, Q. Song, P. Cornillon, M. Spall, and S. Minobe (2008), Air-sea interaction over ocean fronts and eddies, *Dyn. Atmos. Oceans*, *45*, 274–319.

Snyder, M. A., J. L. Bell, L. C. Sloan, P. B. Duffy, and B. Govindasamy (2002), Climate responses to a doubling of atmospheric carbon dioxide for a climatically vulnerable region, *Geophys. Res. Lett.*, *29*, 1514, doi:10.1029/2001GL014431.

Snyder, M. A., L. C. Sloan, N. S. Diffenbaugh, and J. L. Bell (2003), Future climate change and upwelling in the California Current, *Geophys. Res. Lett.*, *30*, 1823, doi:10.1029/2003GL017647.

Steinacher, M., F. Joos, T. L. Frölicher, L. Bopp, P. Cadule, S.C. Doney, M. Gehlen, B. Schneider, and J. Segschneider (2010), Projected 21st century decrease in marine productivity: A multi-model analysis, *Biogeosciences*, *7*, 979–1005.

Strub, P. T., J. M. Mesias, V. Montecino, J. Rutllant, and S. Salinas (1998), Coastal ocean circulation off western South America, in *The Sea*, vol. 11, edited by A. R. Robinson and K. H. Brink, pp. 273–314, John Wiley, New York, NY.

Sutton, R. T., B. Dong, and J. M. Gregory (2007), Land/sea warming ratio in response to climate change: IPCC-AR4 model results and comparison with observations, *Geophys. Res. Lett.*, 34, L02701, doi:10.1029/2006GL028164.

Takahashi, K., and D. S. Battisti (2007a), Processes controlling the mean tropical Pacific precipitation pattern. Part I: The Andes and the eastern Pacific ITCZ, *J. Clim.*, *20*, 3,434–3,451.

Takahashi, K., and D. S. Battisti (2007b), Processes controlling the mean tropical Pacific precipitation pattern. Part II: The SPCZ and the southeast Pacific dry zone, *J. Clim.*, *20*, 5,696–5,706.

Tokinaga, H., and S.-P. Xie (2011), Wave and Anemometer-based Sea-surface Wind (WASWind) for climate change analysis, *J. Clim.*, *24*, 267–285.

Tokinaga, H., S.-P. Xie, A. Timmermann, S. McGregor, T. Ogata, H. Kubota, and Y. M. Okumura (2012a), Regional Patterns of tropical Indo-Pacific climate change: Evidence of the Walker Circulation weakening, *J. Clim.*, *25*, 1,689–1,710, doi:10.1175/JCLI-D-11-00263.1.

Tokinaga, H., S.-P. Xie, C. Deser, Y. Kosaka, and Y. M. Okumura (2012b), Slowdown of the Walker circulation driven by tropical Indo-Pacific warming, *Nature*, *491*, 439–443, doi:10.1038/nature11576.

Vargas, G., S. Pantoja, J. Rutllant, C. Lange, and L. Ortlieb (2007), Enhancement of coastal upwelling and interdecadal ENSO-like variability in the Peru-Chile Current since late 19th century, *Geophys. Res. Lett.*, 34, L13607, doi:10.1029/2006GL028812.

Vecchi, G. A., and B. J. Soden (2007), Global warming and the weakening of the tropical Pacific circulation, *J. Clim.*, *20*, 4,316–4,340, doi:10.1175/JCLI4258.1.

Vecchi, G. A., B. J. Soden, A. T. Wittenberg, I. M. Held, A. Leetmaa, and M. J. Harrison (2006), Weakening of tropical Pacific atmospheric circulation due to anthropogenic forcing, *Nature*, *327*, 216–219, doi:10.1038/nature04744.

Winant, C. D., C. Dorman, C. Friehe, and R. Beardsley (1988), The marine layer off northern California: An example of supercritical channel flow, *J. Atmos. Sci.*, *45*, 3588–3605.

Wyant, M. C., et al. (2010), The PreVOCA experiment: Modeling the lower troposphere in the Southeast Pacific, *Atmos. Chem. Phys.*, *10*, 4,757–4,774, doi:10.5194/acp-10-4757-2010.

Wyrtki, K. (1975), El Niño – The dynamic response of the equatorial Pacific Ocean to atmospheric forcing, *J. Phys. Oceanogr.*, *5*, 572–584.

Xie, S.-P., and S. G. H. Philander (1994), A coupled ocean-atmosphere model of relevance to the ITCZ in the eastern Pacific, *Tellus*, *46A*, 340–350.

Xu, H., Y. Wang, and S.-P. Xie (2004), Effects of the Andes on eastern Pacific climate: A regional atmospheric model study, *J. Clim.*, *17*, 589–602.

Zhang, R., and T. L. Delworth (2005), Simulated tropical response to a substantial weakening of the Atlantic thermohaline circulation, *J. Clim.*, *18*(12), 1853–1860.

## Tables

| CGCM Name | Modeling Group | Atmospheric Model Horizontal Resolution |
|---|---|---|
| CCCma CGCM3.1 | CCCma (Canada) | 3.75°x3.71° |
| CNRM-CM3 | Météo France/CNRM (France) | 2.81°x2.79° |
| GFDL CM2.0 | NOAA/GFDL (United States) | 2.5°x2° |
| GFDL CM2.1 | NOAA/GFDL (United States) | 2.5°x2.02° |
| GISS-ER | NASA GISS (United States) | 5°x4° |
| INM-CM3.0 | INM (Russia) | 5°x4° |
| IPSL-CM4 | IPSL (France) | 3.75°x2.54° |
| MIROC3.2(medres) | CCSR/NIES/FRCGC (Japan) | 2.81°x2.79° |
| MIUB-ECHO-G | MIUB (Germany) | 3.75°x3.71° |
| MPI ECHAM5 | MPI (Germany) | 1.88°x1.87° |
| MRI CGCM2.3.2A | MRI (Japan) | 2.81°x2.79° |
| UKMO-HadGEM1 | Met Office (United Kingdom) | 1.875°x1.25° |

**Table 1** The CGCMs considered in this study. Resolutions are given along the equator.

| Configuration name | LMDz-ESP05 | LMDz-SA1 |
|---|---|---|
| Model setup | Global, variable resolution | Global, 2-way nesting |
| High-resolution region | Eastern South Pacific (99°W–61°W,36°S–6°N) | South America (96°W-14°W, 64°S-19°N) |
| Highest resolution | 0.5° | 1° |
| Scenarios | CR, PI, $2CO_2$, $4CO_2$ (i.e. 20C3M, PIcntrl, stabilized 1pctto2x, stabilized 1pctto4x) | CR, FSSTG (i.e. 20C3M, SRES A1B) |
| Type of experiment | 10-year runs | Seasonal NDJF ensembles |
| SST anomalies added to AMIP | IPSL-CM4 CMIP3 scenarios | CMIP3 CGCM average |

**Table 2** Comparison of the two LMDz configurations and experimental setup used.

## Figure Captions

**Fig. 1** 1950-2009 trend in corrected vector and scalar wind ($10^{-2}$ m $s^{-1}$ $yr^{-1}$) from the WASWind product [*Tokinaga and Xie*, 2011]. Only grid cells with data available for 98% of the time or more are shown. No offshore data is available due to the lack of ship tracks in this region.

**Fig. 2** Linear trend in alongshore monthly surface wind near the coast ($10^{-2}$ m $s^{-1}$ $yr^{-1}$) in the PCUS for 12 CGCMs (table 1) with increasing $CO_2$ concentrations in the $4CO_2$ scenario (see text) in (a) summer (December through February) and (b) winter (June through August). Winds from all the CGCMs are previously interpolated bilinearly onto a common 1°x1° grid. The alongshore direction and nearshore area (typically 1-2° wide) are determined using the land-sea mask. Note that the IPSL-CM4 model (orange curve) agrees well with the ensemble mean over the 12 CGCMs (thick black curve) except south of 30-35°S where it underestimates the wind increase

**Fig. 3** GCM grid for (a) LMDz-ESP05 and (b) LMDz-SA1. The red box on each panel indicates the limits of the zoomed grid.

**Fig. 4** Mean surface wind (m $s^{-1}$) from (a) IPSL-CM4 in the 20C3M scenario (1990-1999), (b) LMDz-ESP05 in the CR, and (c) the SCOW (2000-2008). Shading and contours are for wind, arrows are for wind vectors. For clarity, only one arrow was drawn for every 16 and 64 grid points in (b) and (c), respectively

**Fig. 5** Mean alongshore wind (shading, m $s^{-1}$) and air temperature (contours, °C) vertical, cross-shore structures (a), (b) in winter (April-September) off Peru (15°S) and (c), (d) in summer (October-March) off Chile (35°S) for (a), (c) LMDz-ESP05 and (b), (d) ERA-Interim. Positive alongshore wind values are for equatorward wind. The alongshore direction is roughly estimated as directed along the northwest/southeast direction at 15°S and as meridional at 35°S

**Fig. 6** LMDz-ESP05 sea level pressure (hPa) and surface wind anomaly (m $s^{-1}$) with respect to PI in summer (December-February) for (a) $2CO_2$ and (b) $4CO_2$; in winter (June-August) for (c) $2CO_2$ and (d) $4CO_2$. Shading is for anomalous wind, arrows are for anomalous wind vectors, red contours are for sea level pressure. PI sea level pressure is also shown (white contours). For clarity, only one arrow was drawn for every 16 grid points. A background value of 1000 hPa was substracted from sea level pressure values

**Fig. 7** (a) Annual mean LMDz-ESP05 wind stress curl in the PI scenario; wind stress curl difference: (b) 2CO2-PI; (c) 4CO2-PI. Negative wind stress curl indicates upwelling. Units are $10^{-7}$ N $m^{-2}$

**Fig. 8** (a) Mean LMDz-ESP05 alongshore wind along the coast (m $s^{-1}$) for PI (blue), $2CO_2$ (purple), and $4CO_2$ (red). (b) Mean LMDz-ESP05 alongshore momentum balance along the coast ($10^{-4}$ m $s^{-2}$) for PI (blue) and $4CO_2$ (red). $2CO_2$ is omitted for clarity. The Coriolis term is marked by a solid line, the sum of the advection terms by a dotted line, the alongshore pressure gradient term by a dashed line, and the friction term by a dash-dotted line. (c) Mean LMDz-ESP05 cross-shore temperature gradient along the coast ($10^{-2}$ °C $km^{-1}$) for PI (blue), $2CO_2$ (purple), and $4CO_2$

(red). All quantities were computed in a one-degree coastal band using the land-sea mask to determine the alongshore and cross-shore directions (see text)

**Fig. 9** Surface wind (m $s^{-1}$) in summer (December-February) from (a) LMDz-SA1 in the CR, (b) LMDz-ESP05 in the CR, and (c) the SCOW (2000-2008). (d) Alongshore wind in a one-degree band along the coast (m $s^{-1}$) in summer for LMDz-ESP05 (red), LMDz-SA1 (green), and SCOW (blue). Shading and contours are for wind, arrows are for wind vectors on (a-c). For clarity, only one arrow was drawn for every 4, 16, and 64 grid points in (a), (b), and (c), respectively

**Fig. 10** Same as Fig. 5, except in DJF for (a,c) LMDz-SA1 and (b,d) ERA-Interim, at (a,b) 15°S and (c,d) 30°S

**Fig. 11** (a) LMDz-SA1 FSSTG sea level pressure (hPa) and surface wind anomaly (m $s^{-1}$) with respect to CR in summer (December-February). Shading is for anomalous wind, arrows are for anomalous wind vectors, red contours are for sea level pressure. CR sea level pressure is also shown (white contours). For clarity, only one arrow was drawn for every 4 grid points. A background value of 1000 hPa was substracted from sea level pressure values. (b) Mean LMDz-SA1 alongshore momentum balance along the coast ($10^{-4}$ m $s^{-2}$) for CR (blue) and FSSTG (red). The different terms are labelled as in Fig. 8b

**Fig. 12** Linear trend in monthly surface wind ($10^{-2}$ m $s^{-1}$ $yr^{-1}$), precipitation ($10^{-2}$ mm $day^{-1}$ $yr^{-1}$), and land/sea surface temperature ($10^{-2}$ °C $yr^{-1}$) in the PCUS for 12 CGCMs (table 1) with increasing $CO_2$ concentrations in the $4CO_2$ scenario. Shading is for trends in precipitation, arrows are for trends in wind vectors, white contours are for trends in surface temperature

**Fig. 13** LMDz-ESP05 $4CO_2$ surface wind anomaly (m $s^{-1}$) and precipitation anomaly (mm $day^{-1}$) with respect to PI (a) in summer (December-February) and (b) in winter (June-August). Shading and contours are for anomalous precipitation, arrows are for anomalous wind vectors. For clarity, only one arrow was drawn for every 16 grid points

**Fig. 14** (a-d) LMDz-ESP05 PI vorticity balance and $4CO_2$ anomaly with respect to PI ($10^{-10}$ $s^{-2}$) off Peru in DJF. Note that (a) corresponds to $\beta V$ and that (a) ≈ (b) + (c) + (d). (e-h) Same as (a-d) except for LMDz-SA1 CR vorticity balance and FSSTG anomaly with respect to CR. Shading is for anomalous vorticity terms, contours are for DJF PI (a-d) and CR (e-h) vorticity terms

Figure 1

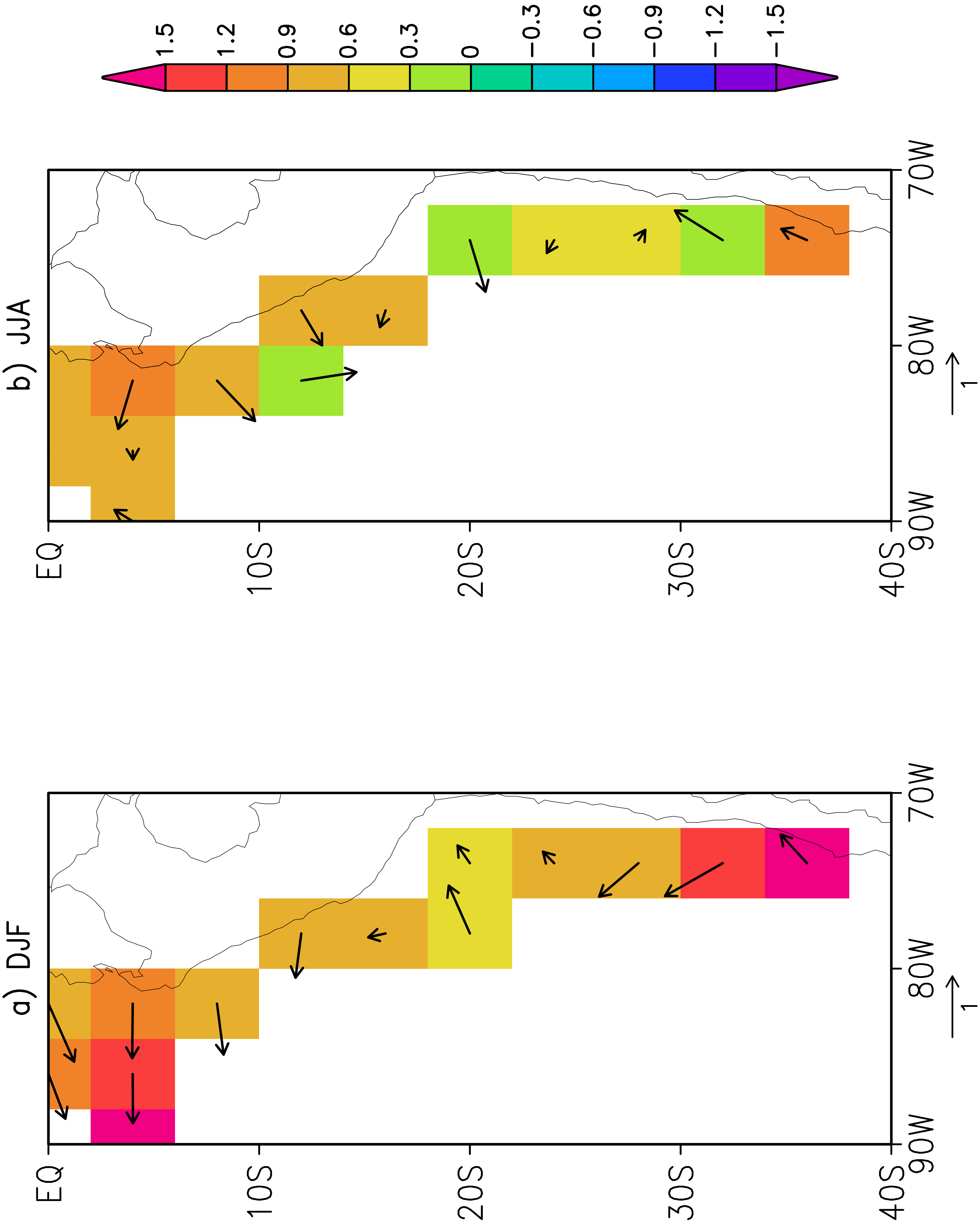

a) DJF
b) JJA
EQ
10S
20S
30S
40S
90W
80W
70W
1
1.5
1.2
0.9
0.6
0.3
0
−0.3
−0.6
−0.9
−1.2
−1.5

Figure 2

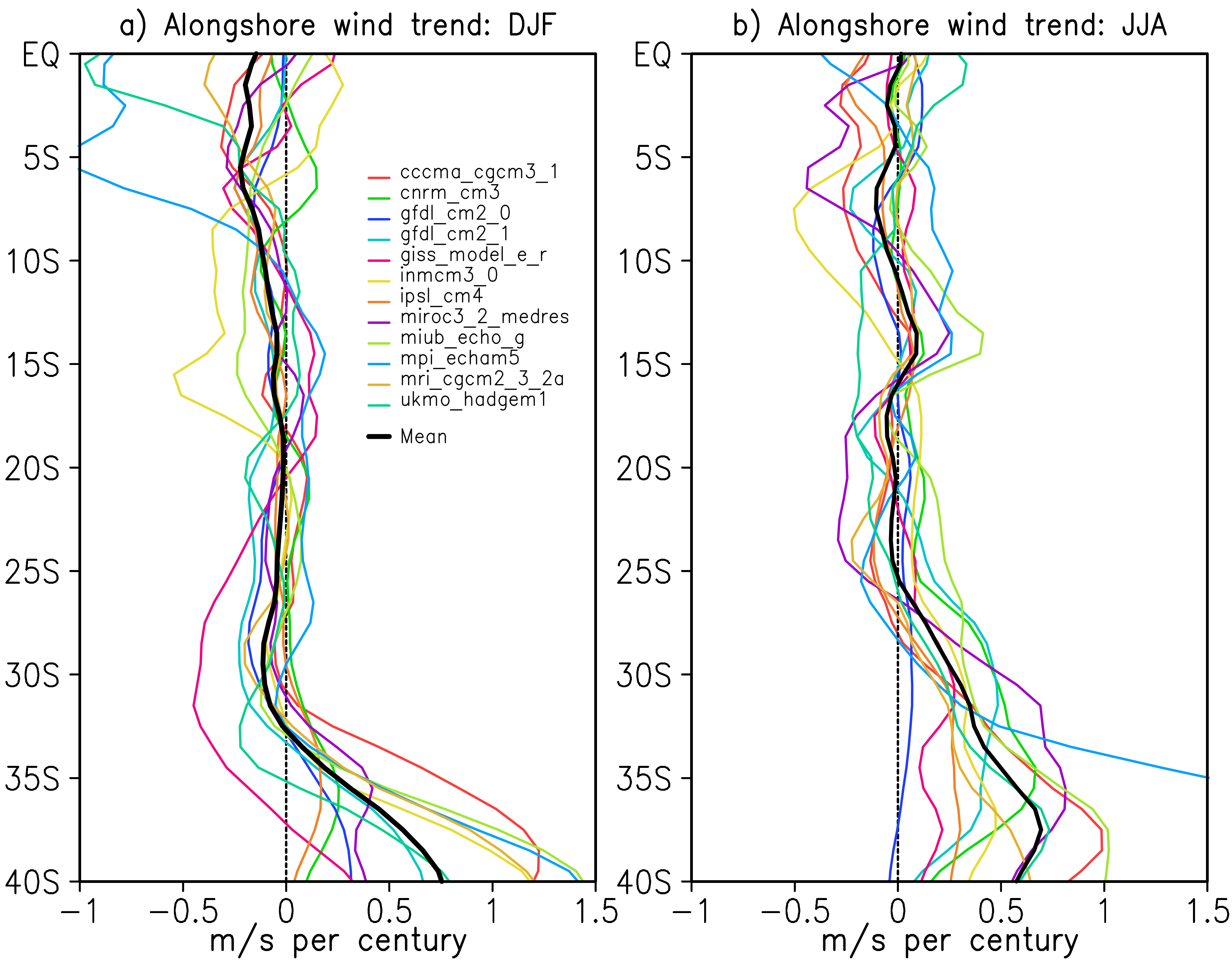
a) Alongshore wind trend: DJF
b) Alongshore wind trend: JJA
EQ
5S
10S
15S
20S
25S
30S
35S
40S
−1
−0.5
0
0.5
1
1.5
m/s per century
cccma_cgcm3_1
cnrm_cm3
gfdl_cm2_0
gfdl_cm2_1
giss_model_e_r
inmcm3_0
ipsl_cm4
miroc3_2_medres
miub_echo_g
mpi_echam5
mri_cgcm2_3_2a
ukmo_hadgem1
Mean

Figure 3

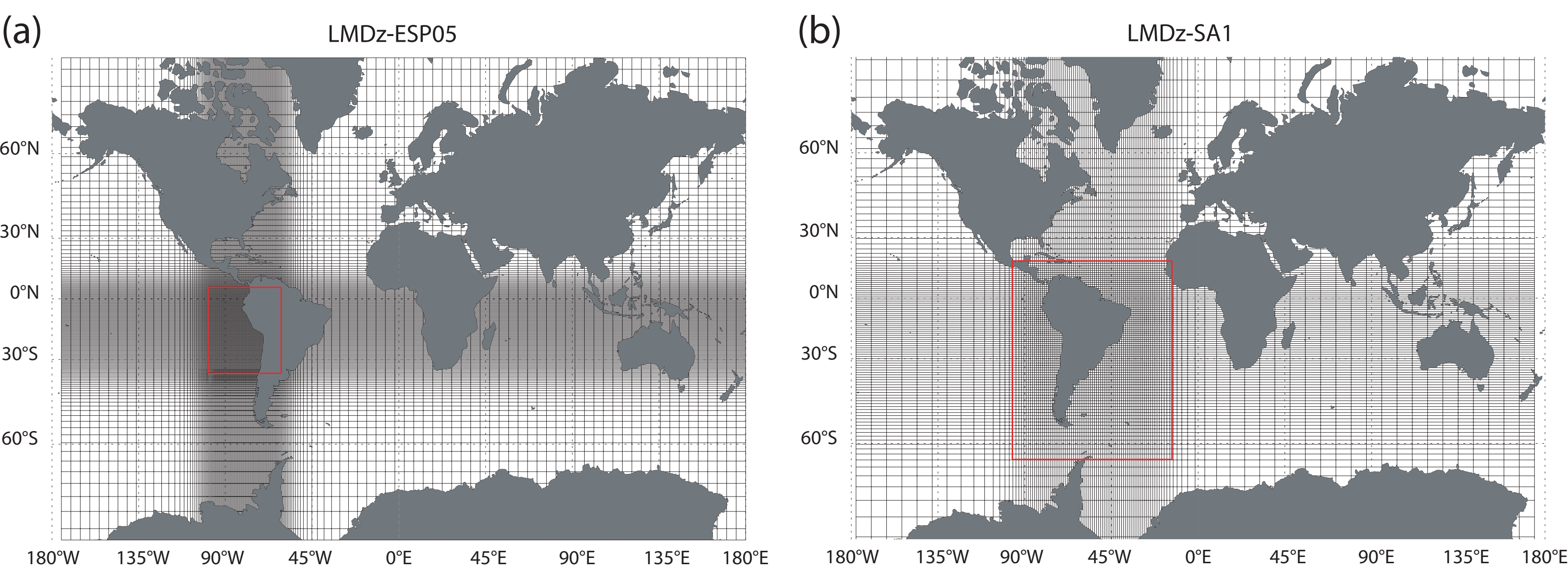
(a)
LMDz-ESP05
60°N
30°N
0°N
30°S
60°S
180°W
135°W
90°W
45°W
0°E
45°E
90°E
135°E
180°E
(b)
LMDz-SA1
60°N
30°N
0°N
30°S
60°S
180°W
135°W
90°W
45°W
0°E
45°E
90°E
135°E
180°E

Figure 4

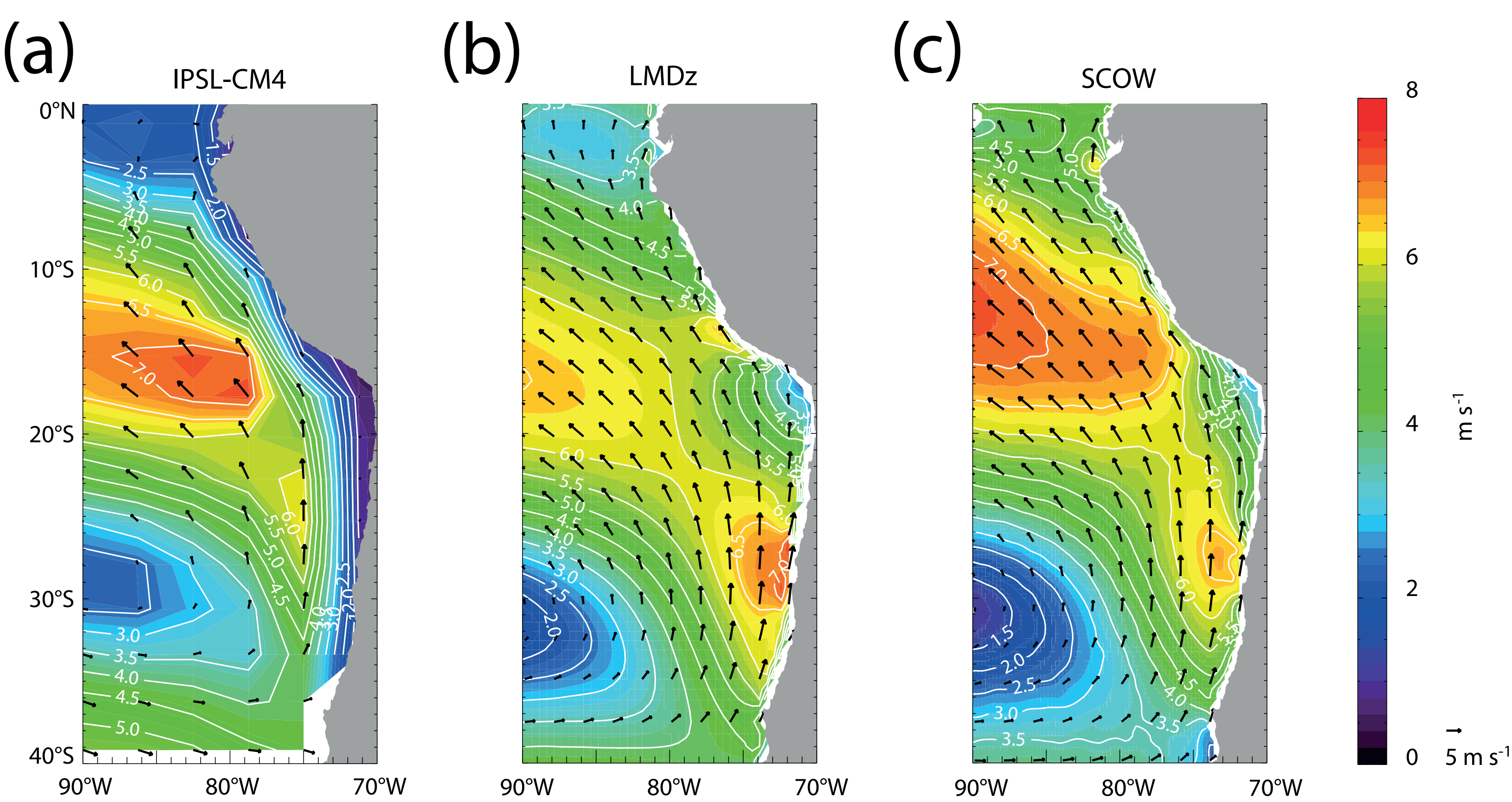

(a)
IPSL-CM4
(b)
LMDz
(c)
SCOW
0°N
10°S
20°S
30°S
40°S
90°W
80°W
70°W
8
6
4
2
0
m s-1
5 m s-1

Figure 5

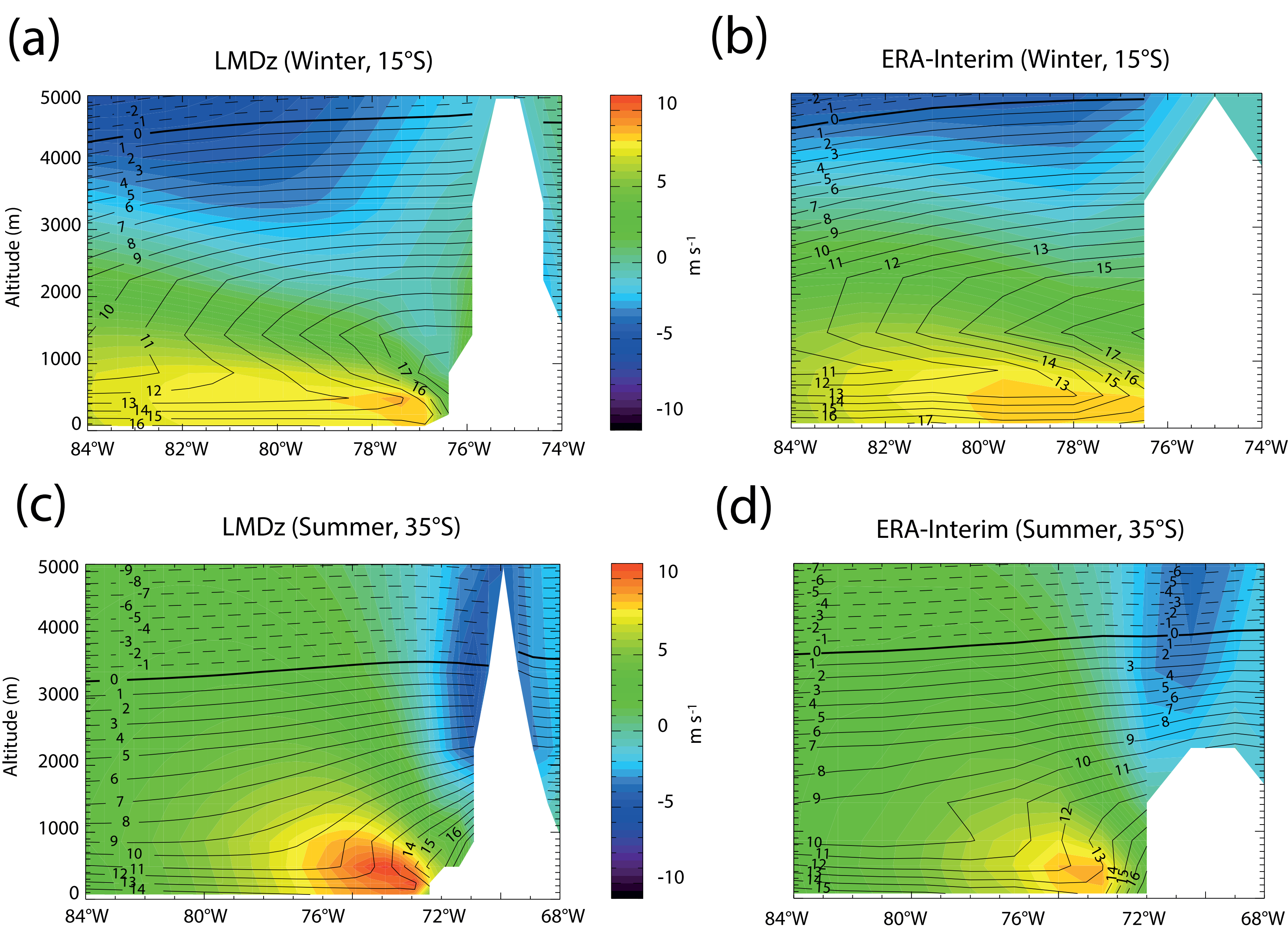
(a)
LMDz (Winter, 15°S)
(b)
ERA-Interim (Winter, 15°S)
(c)
LMDz (Summer, 35°S)
(d)
ERA-Interim (Summer, 35°S)
Altitude (m)
m s-1
84°W
82°W
80°W
78°W
76°W
74°W
72°W
68°W

Figure 6

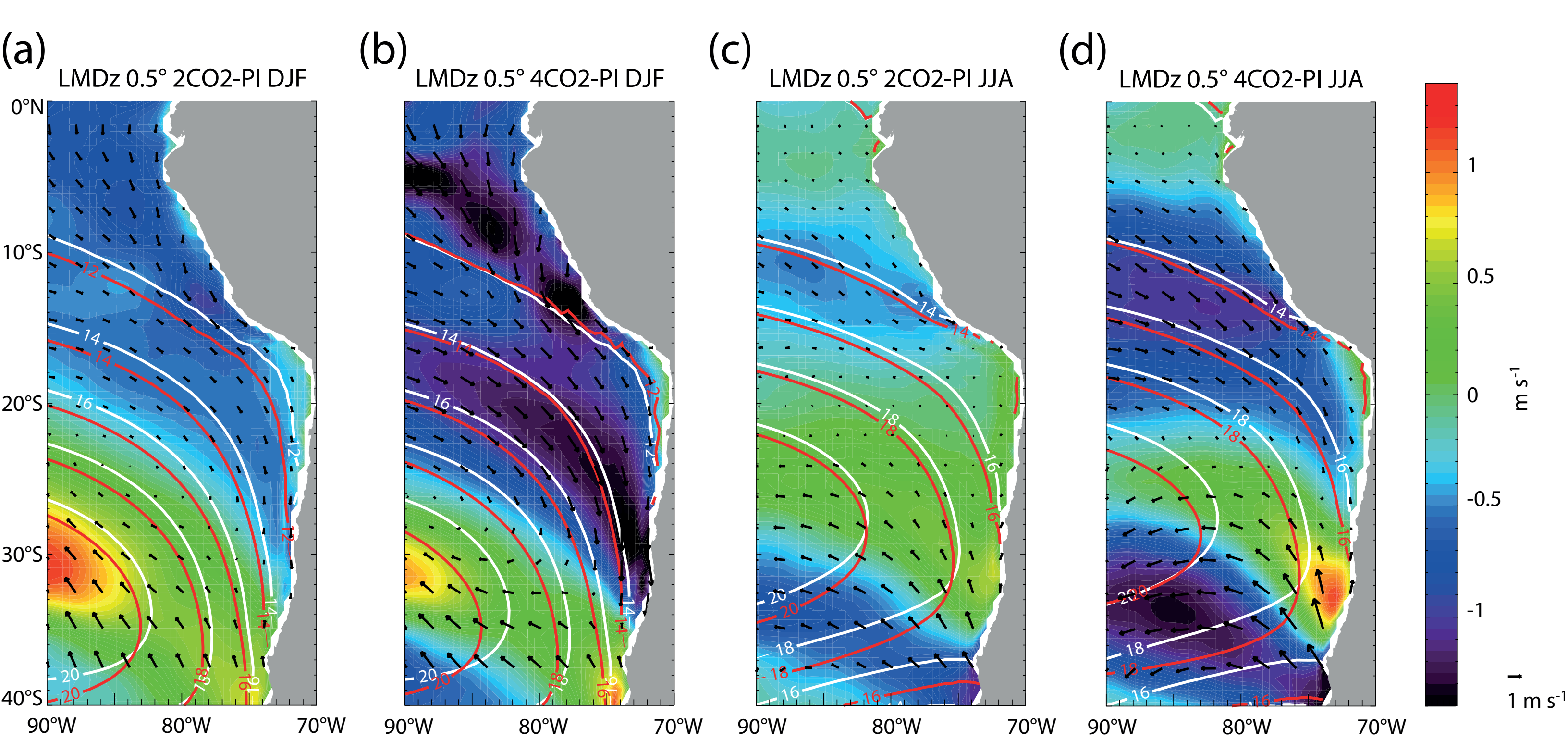

(a)
LMDz 0.5° 2CO2-PI DJF
(b)
LMDz 0.5° 4CO2-PI DJF
(c)
LMDz 0.5° 2CO2-PI JJA
(d)
LMDz 0.5° 4CO2-PI JJA
0°N
10°S
20°S
30°S
40°S
90°W
80°W
70°W
1
0.5
0
-0.5
-1
m s-1
1 m s-1

Figure 7

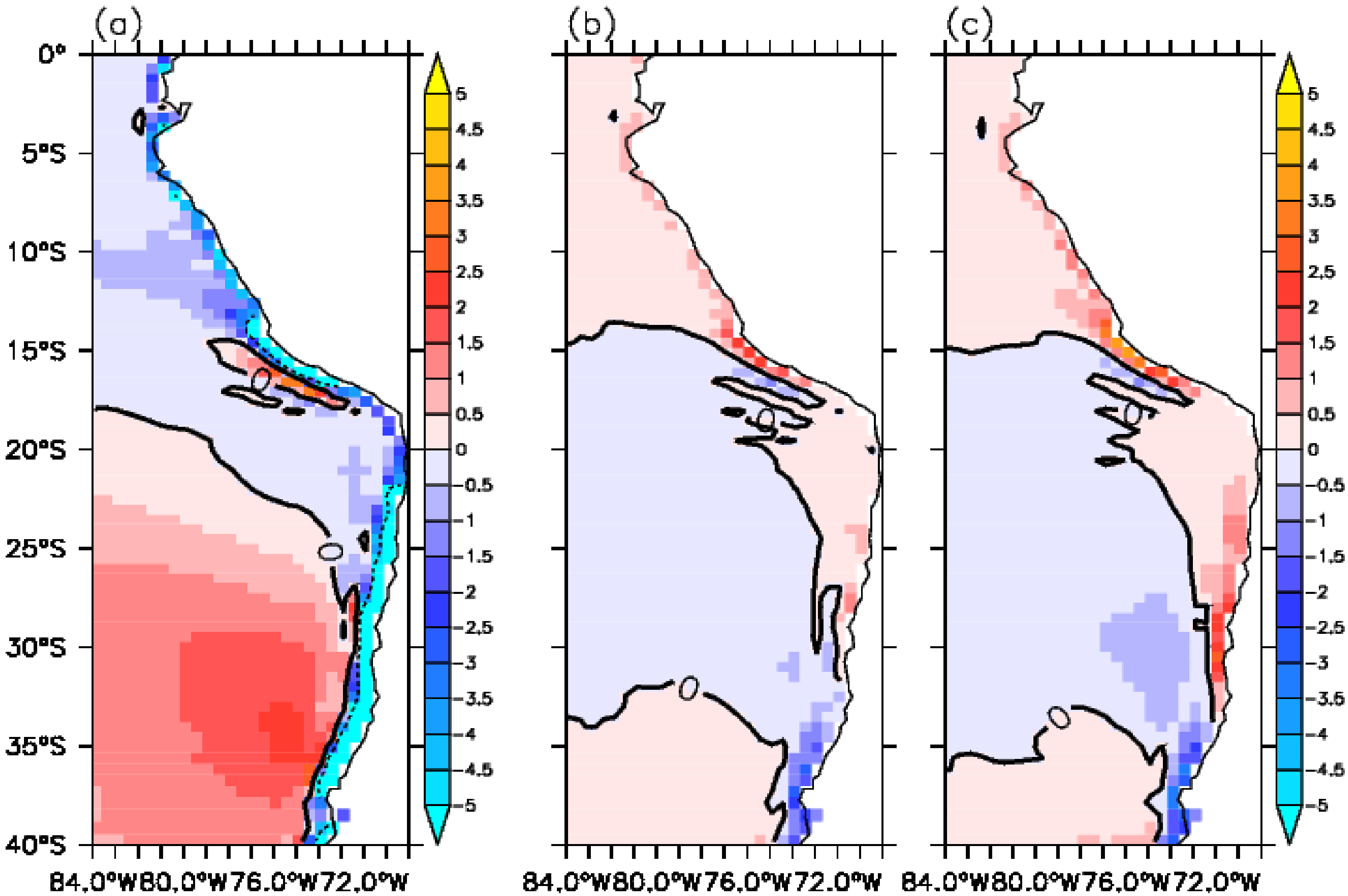

(a)
(b)
(c)
0°
5°S
10°S
15°S
20°S
25°S
30°S
35°S
40°S
84.0°W80.0°W76.0°W72.0°W
84.0°W80.0°W76.0°W72.0°W
84.0°W80.0°W76.0°W72.0°W
5
4.5
4
3.5
3
2.5
2
1.5
1
0.5
0
-0.5
-1
-1.5
-2
-2.5
-3
-3.5
-4
-4.5
-5

Figure 8

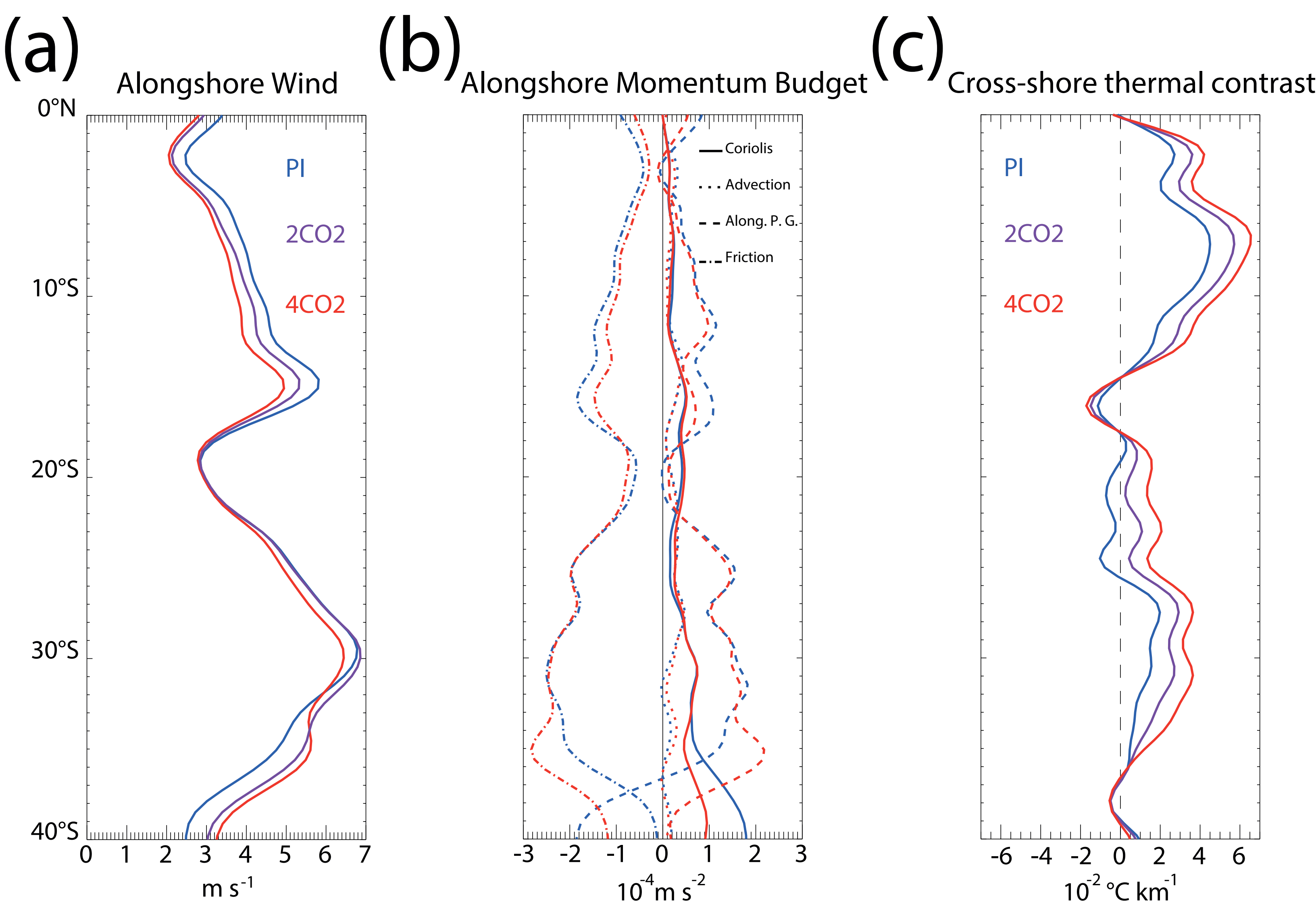

(a)
Alongshore Wind
0°N
10°S
20°S
30°S
40°S
PI
2CO2
4CO2
0 1 2 3 4 5 6 7
m s-1
(b)
Alongshore Momentum Budget
Coriolis
Advection
Along. P. G.
Friction
-3 -2 -1 0 1 2 3
10-4 m s-2
(c)
Cross-shore thermal contrast
PI
2CO2
4CO2
-6 -4 -2 0 2 4 6
10-2 °C km-1

Figure 9

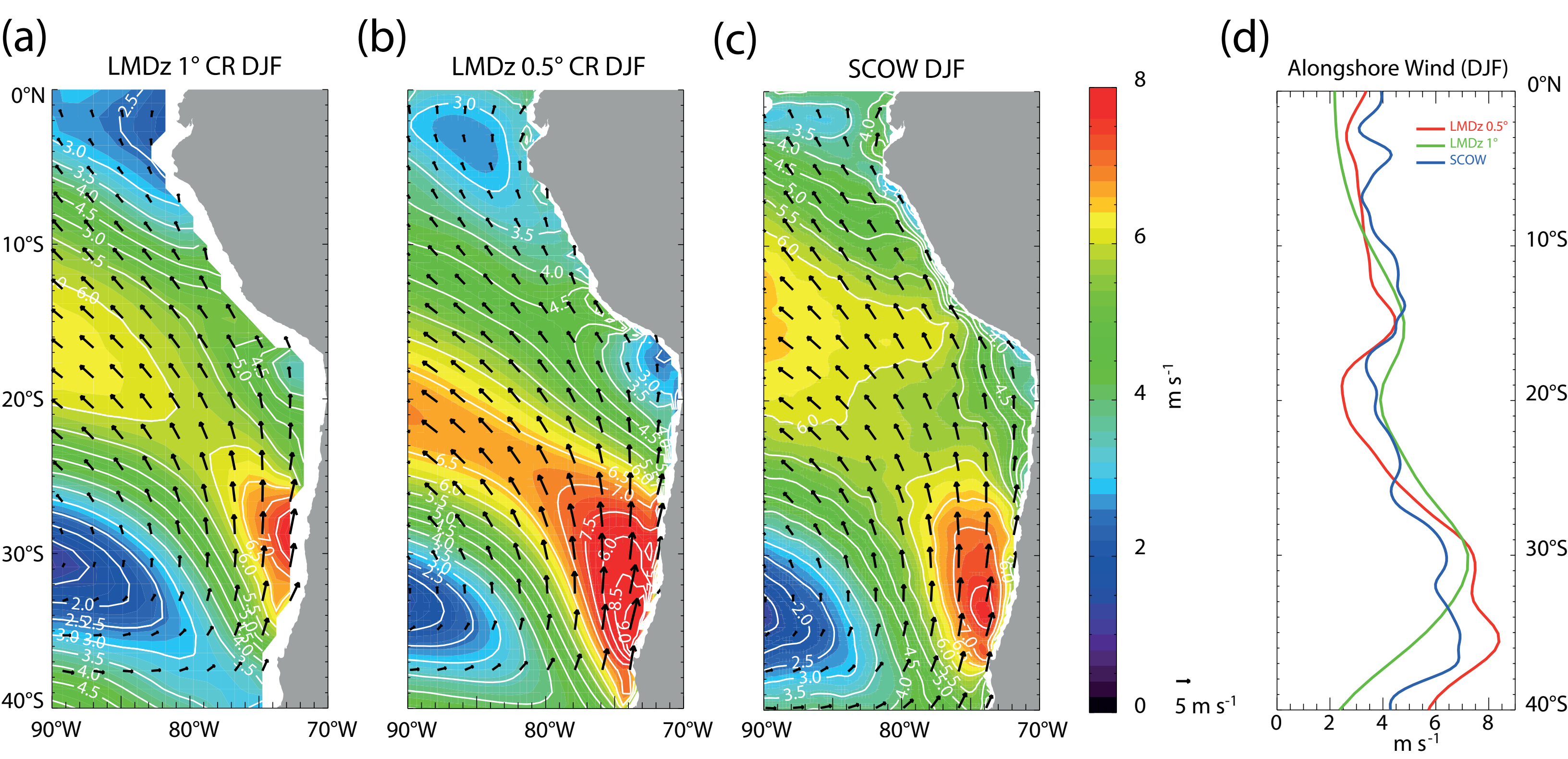

(a)
LMDz 1° CR DJF
(b)
LMDz 0.5° CR DJF
(c)
SCOW DJF
(d)
Alongshore Wind (DJF)
LMDz 0.5°
LMDz 1°
SCOW
0°N
10°S
20°S
30°S
40°S
90°W
80°W
70°W
m s-1
5 m s-1

Figure 10

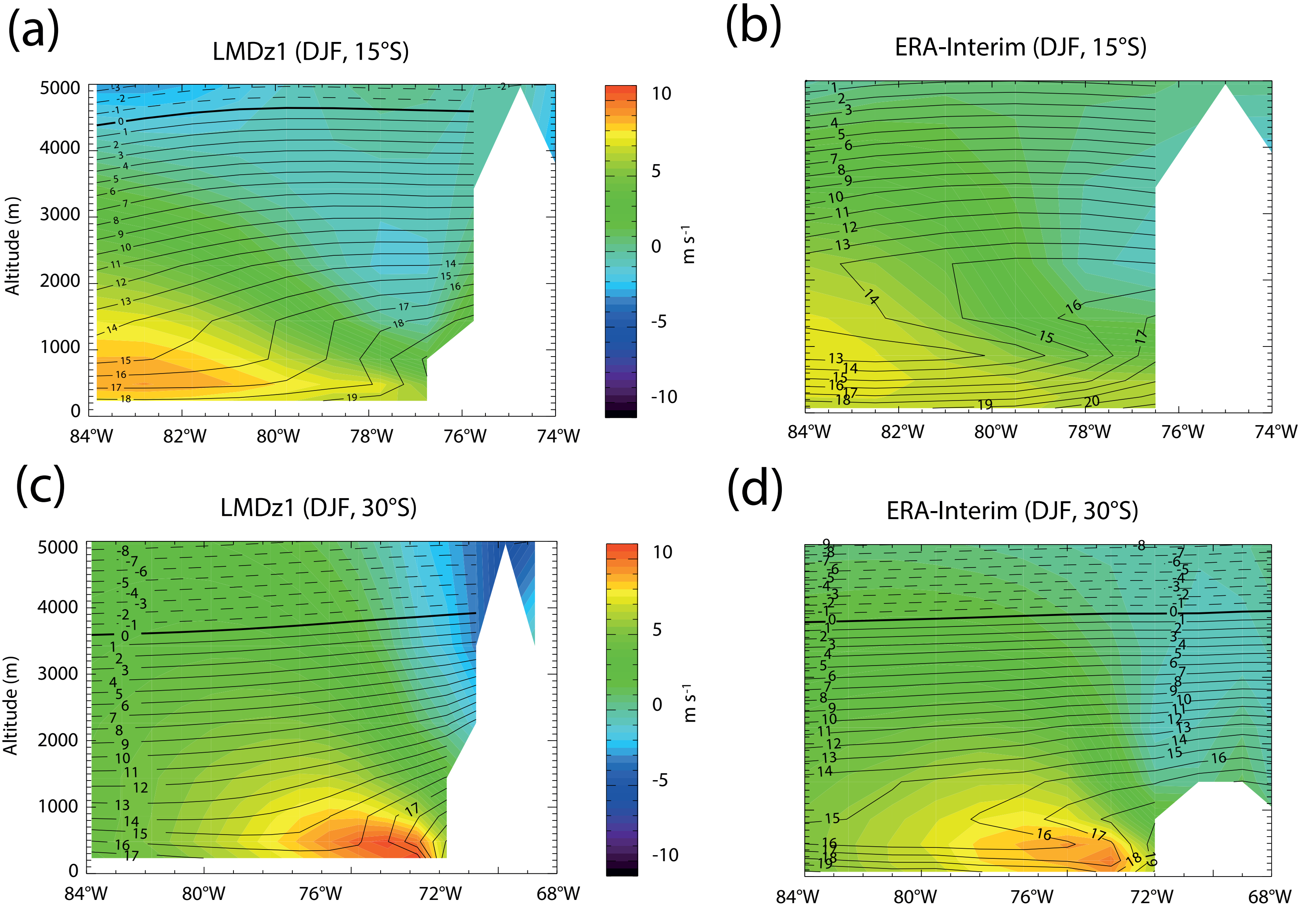
(a)
LMDz1 (DJF, 15°S)
(b)
ERA-Interim (DJF, 15°S)
(c)
LMDz1 (DJF, 30°S)
(d)
ERA-Interim (DJF, 30°S)
Altitude (m)
0
1000
2000
3000
4000
5000
84°W
82°W
80°W
78°W
76°W
74°W
72°W
68°W
m s-1
10
5
0
-5
-10

Figure 11

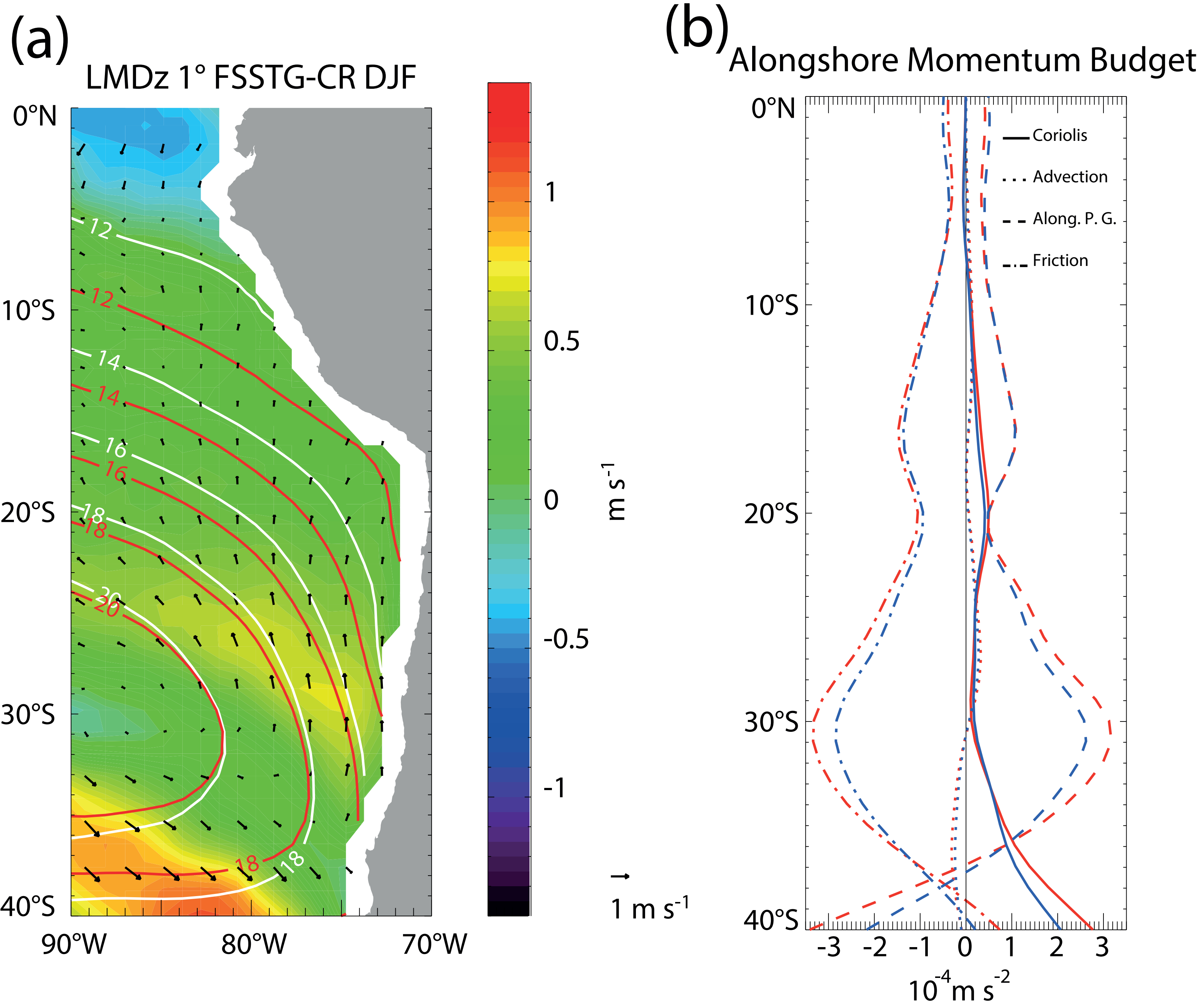

(a)
LMDz 1° FSSTG-CR DJF
0°N
10°S
20°S
30°S
40°S
90°W
80°W
70°W
12
14
16
18
20
m s-1
1 m s-1
(b)
Alongshore Momentum Budget
Coriolis
Advection
Along. P. G.
Friction
-3 -2 -1 0 1 2 3
10-4 m s-2

Figure 12

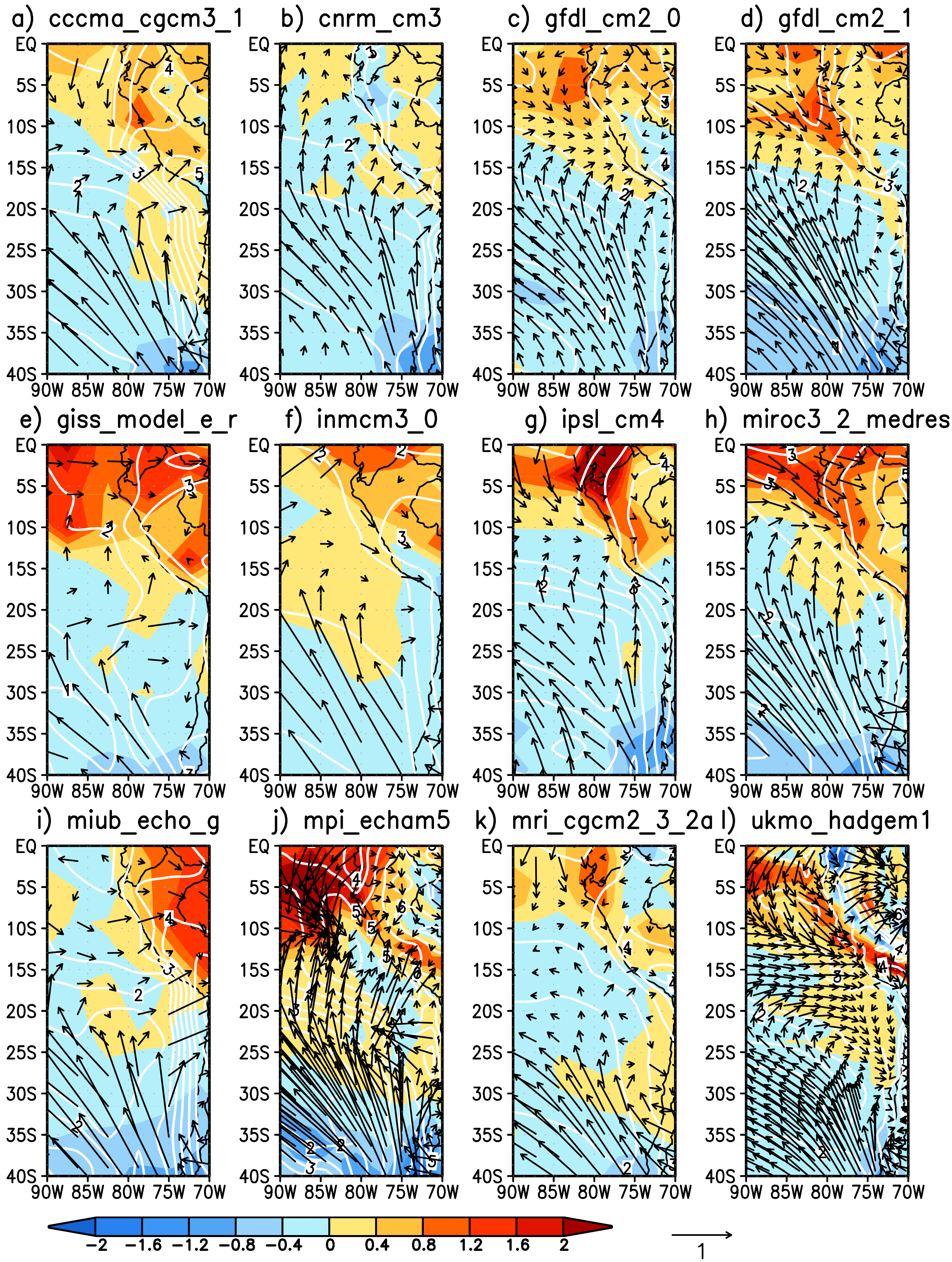

a) cccma_cgcm3_1
b) cnrm_cm3
c) gfdl_cm2_0
d) gfdl_cm2_1
e) giss_model_e_r
f) inmcm3_0
g) ipsl_cm4
h) miroc3_2_medres
i) miub_echo_g
j) mpi_echam5
k) mri_cgcm2_3_2a
l) ukmo_hadgem1
EQ
5S
10S
15S
20S
25S
30S
35S
40S
90W 85W 80W 75W 70W
−2 −1.6 −1.2 −0.8 −0.4 0 0.4 0.8 1.2 1.6 2
1

Figure 13

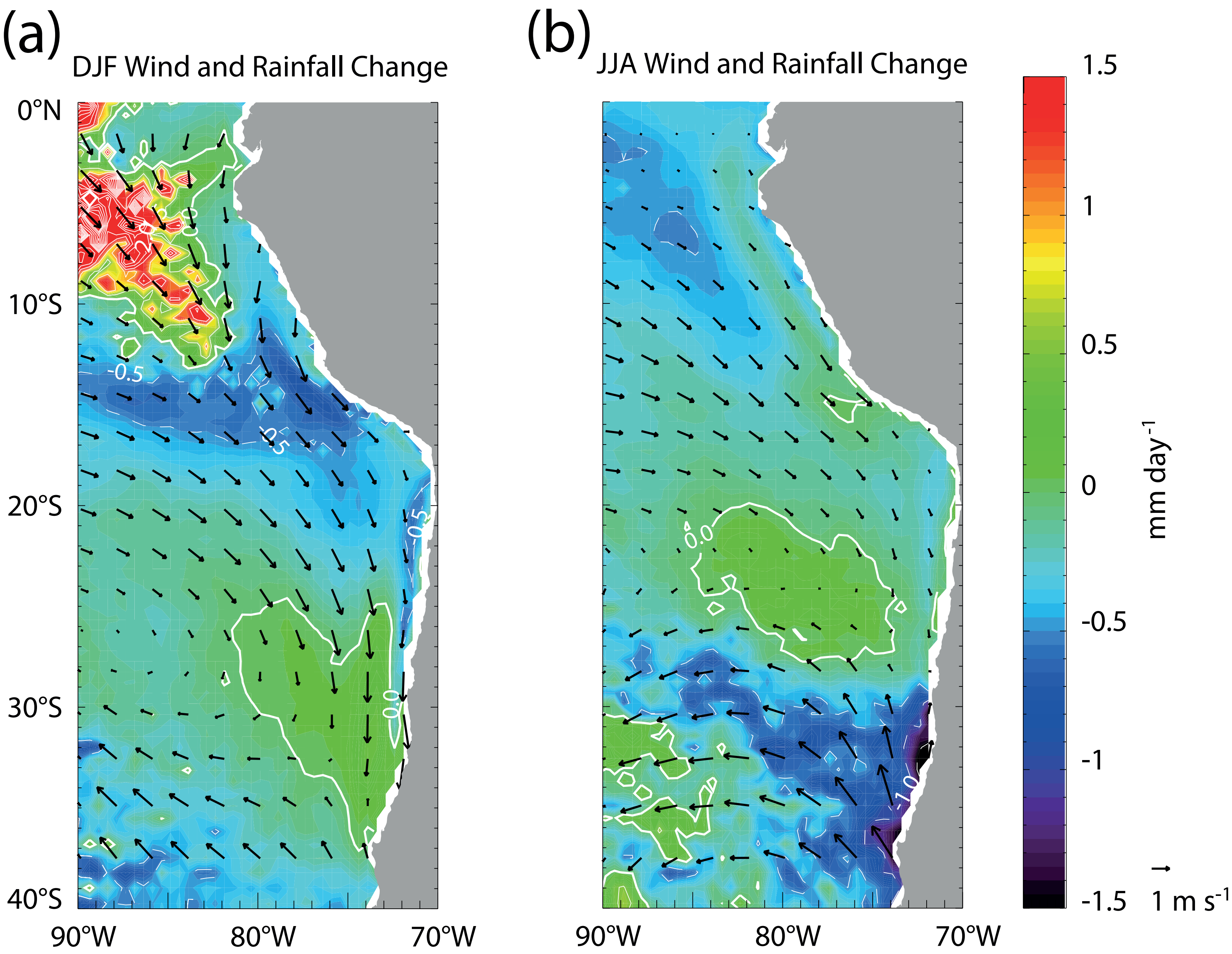
(a)
DJF Wind and Rainfall Change
(b)
JJA Wind and Rainfall Change
0°N
10°S
20°S
30°S
40°S
90°W
80°W
70°W
-0.5
0.0
-1.0
1.5
1
0.5
0
-0.5
-1
-1.5
mm day-1
1 m s-1

Figure 14

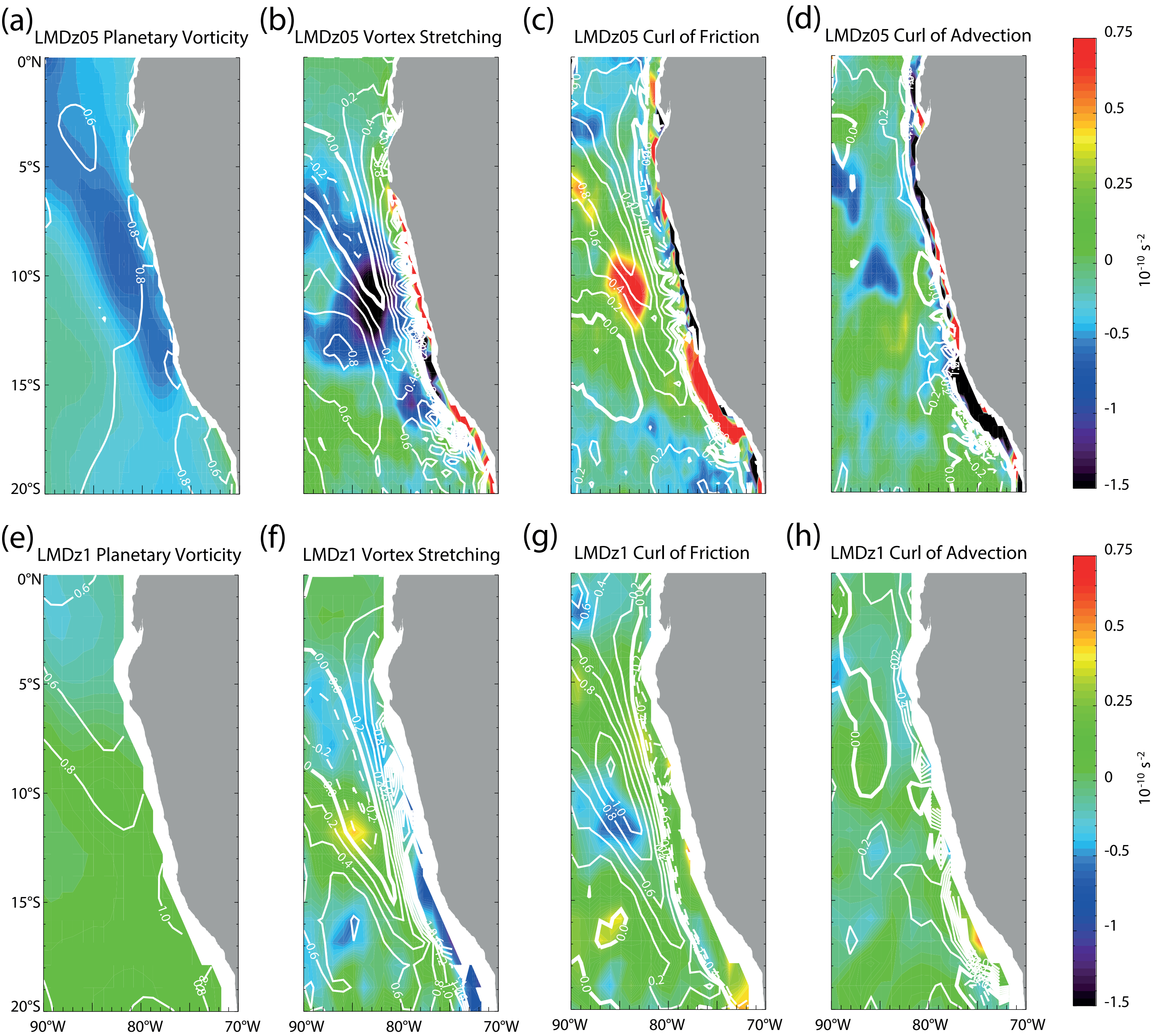
(a) LMDz05 Planetary Vorticity
(b) LMDz05 Vortex Stretching
(c) LMDz05 Curl of Friction
(d) LMDz05 Curl of Advection
(e) LMDz1 Planetary Vorticity
(f) LMDz1 Vortex Stretching
(g) LMDz1 Curl of Friction
(h) LMDz1 Curl of Advection
0°N
5°S
10°S
15°S
20°S
90°W
80°W
70°W
0.75
0.5
0.25
0
-0.5
-1
-1.5
$10^{-10}$ $s^{-2}$